

PART II

5. Hypersonic flow control experiment

5.1 Introduction

The utilization of MHD-interaction in the hypersonic flight has recently received an increasing level of interest. Hypersonic flight regimes occur when a reusable space vehicle re-enters the atmosphere. Another application of the hypersonic flight concerns the development of a single stage to orbit (SSTO) vehicle, which is now one of the main pre-requisite for the commercial exploitation of space flight. An SSTO vehicle should be powered by different stages of air breathing engines, carrying it from the take-off to orbit. In this case an application of the MHD interaction is the control of the shock wave position in the thruster gas inlet. In recent scientific publications on this subject several application of the MHD interaction in hypersonic flows and in the hypersonic flight have been discussed.¹⁻⁹ In the AJAX project MHD techniques are utilized to by-pass kinetic energy of the working fluid from the supersonic diffuser to the nozzle.^{10,11} By doing this, the flow velocity in the combustion chamber is reduced to acceptable values, even for high Mach numbers.

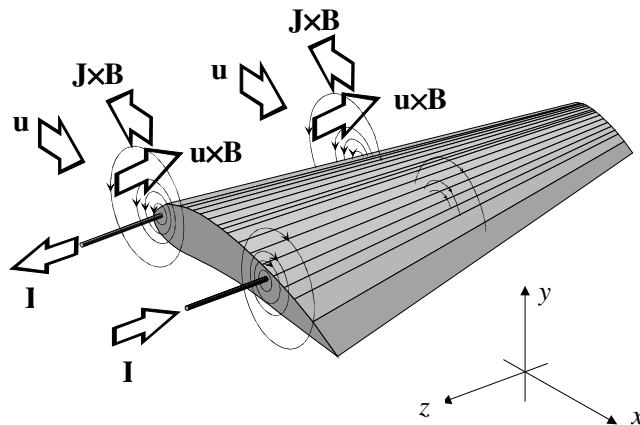


Fig. 5.1: Principles of the magneto hydrodynamic flow control.

In the last years several studies on the interaction of hypersonic flows with plasmas and with the MHD process have been undertaken.¹²⁻¹⁵ These have been focused on the control of the fluid dynamic phenomena in the region between the shock front and the surface of the vehicle and mainly with the control of the thermal fluxes.^{16, 17} Shock layers during hypersonic flight have very remarkable characteristics. When flying at high altitudes and high speeds

(as occurs during re-entry), a gas dynamic shock in front of the vehicle is established. This causes a compression of the gas and a strong heating of it. The temperature reaches values in the range of 10 000 K. Close to the surface the temperature is sufficient to cause ionization of the gas, and to sustain a significant level of MHD interaction process when the magnetic flux density is of the order of the Tesla. Hence this can generate forces which can modify the fluid dynamic configuration and can move the shock front forward from the vehicle surface. This is followed by a decrease of the thermal flux toward the wall and results in thermal protection of the vehicle. Moreover the aerodynamic drag and the vehicle trim will be modified.

5.2 Numerical Simulation

Numerical simulations of magnetohydrodynamic flow control have been carried out by several groups. Here the results of the Bologna unit are shown. A numerical model which describes the MHD flow [15] has been utilized to analyze the magneto hydrodynamic field over a blunt body in a hypersonic regime. The dimensions of the considered body are shown in figure 5.2, where the position of the conductors is shown as well.

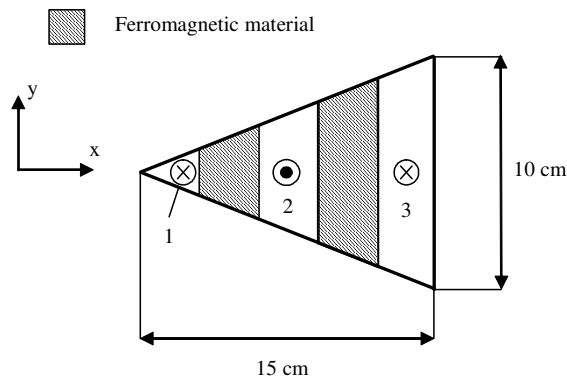


Fig. 5.2: Schematic of the blunt body.

The body considered support a magnetic circuit constituted by a ferromagnetic material. This allows the reduction of the current needed to generate a given magnetic flux, and gives some degree of control of the distribution of the magnetic flux density lines. The conductor windings are deployed so that the total current flowing in the section numbered 2 in figure 5.2 is equal to the sum of the currents flowing in the sections 1 and 3. The distribution of the magnetic flux density produced by the described arrangement is shown in figure 5.3. When the current I_2 is equal to 52 KA, the

magnetic flux density is about 1 T on the surface of the wedge, with a maximum of 2.29 T .

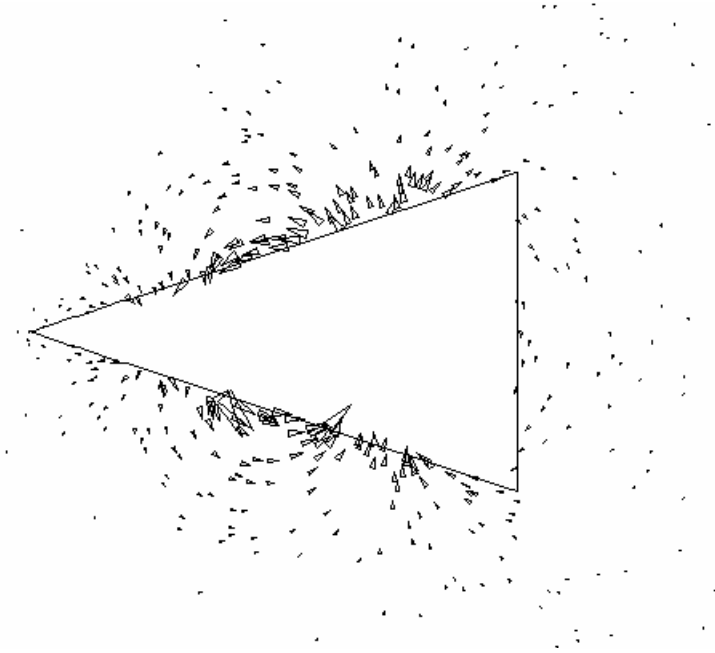


Fig. 5.3: Magnetic flux density around the blunt body.

The circuits can be arranged in a different configuration, shown in figure 5.4. In this arrangement, the magnetic flux density, being confined in the ferromagnetic core, will be almost zero in the lower boundary layer of the wedge. As a consequence, the forces caused by the MHD interaction will act only on the upper side of the wedge.

A free stream flow with a 76 Pa pressure and a 10^{-3} Kg m⁻³ density is considered, in order to simulate the condition of a vehicle at a 50 Km altitude. The calculation of the flow condition around the blunt body has been performed on a 26,000 node unstructured triangular mesh. The calculated Mach isolines, isobars and isothermal distributions when no MHD interaction is present are shown in fig. 5.5.A, 5.5.B, 5.5.C respectively. In order to estimate the conductivity and Hall parameter, a 50 T^{-1} constant electron mobility has been assumed. This value corresponds roughly to the mobility in the boundary layer region. Assuming an ionization degree of 10^{-3} , the higher value of the conductivity is 360 S m^{-1} , in the denser region near the wedge walls.

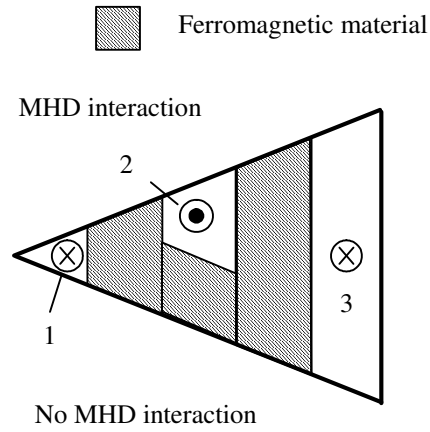


Fig. 5.4: Schematic of the blunt body.

A first calculation was performed in order to evaluate the effects of the MHD interaction when neglecting the Hall current. The calculation results are shown in fig. 5.6.A, 5.6.B, 5.6.C, where Mach isolines, isobars and isothermals are plotted respectively. As can be easily noted, the evaluated MHD interaction strongly affects the flow around the blunt body.

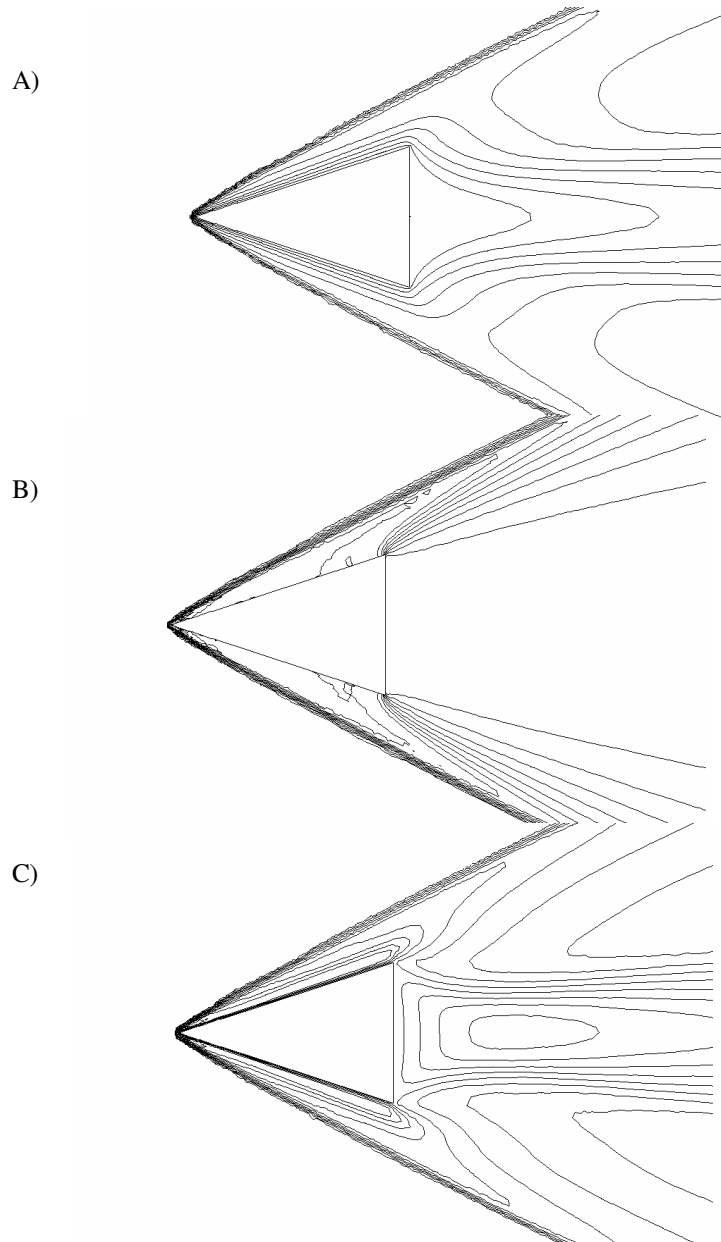


Fig 5.5: A) Mach isolines, B) Pressure isolines C) Temperature isolines with $\mathbf{B}=0$.

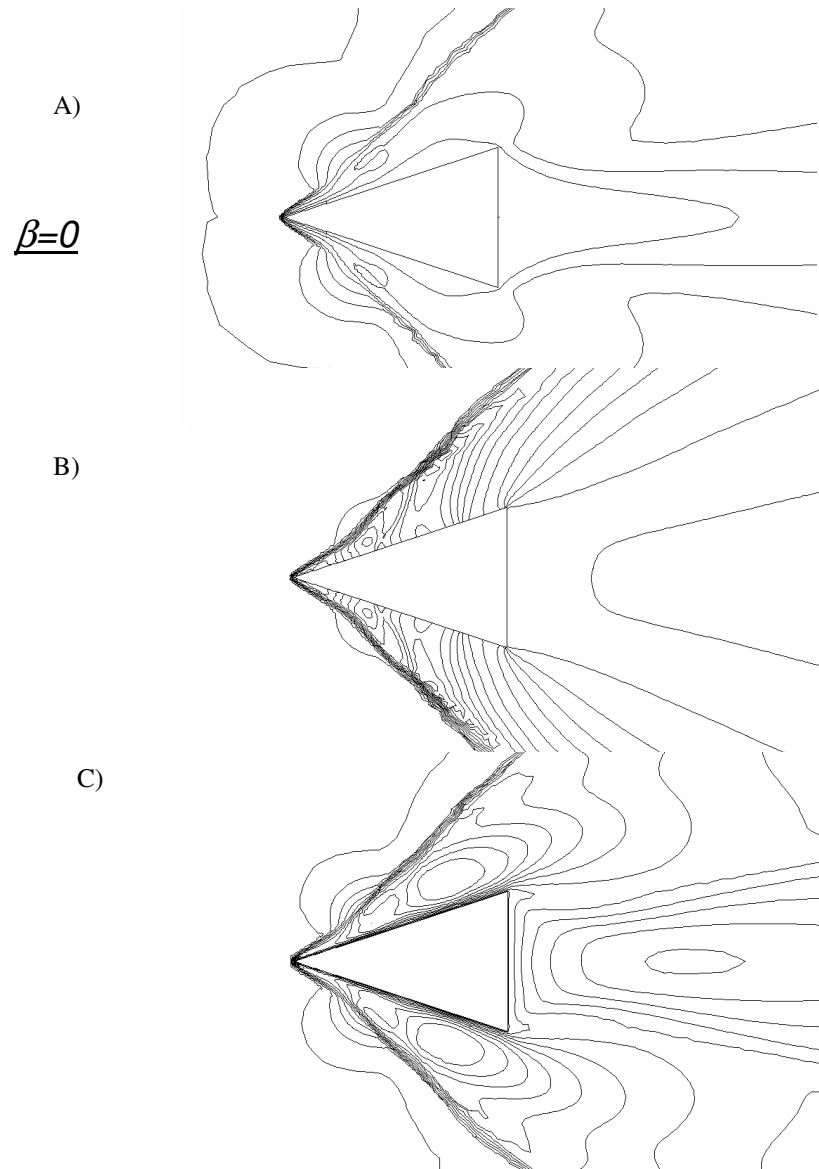


Fig. 5.6: A) *Mach isolines*, B) *Pressure isolines* C) *Temperature isolines* with $B \neq 0$ and $\beta = 0$.

The pressure coefficient PC, defined as the ratio between the gas pressure and the free flow pressure P_{in} is calculated along the body wall in the leading edge region. These results are shown in figure 5.7.A, and compared with the pressure coefficient distribution with no applied magnetic flux density. The leading edge vertex is the origin of the x axis. The reduction of the air speed caused by the

specific force $\mathbf{J} \times \mathbf{B}$ generates a pressure rise along the wedge sides. The integrals of the forces along the direction normal to the wedge sides due to the wall pressure, increases by more than 100%.

In figure 5.7.B, the friction coefficient FC, defined as the ratio between the viscous stress on the wedge wall τ_w and the free flow pressure is plotted along the body wall, with and without the applied magnetic flux density.

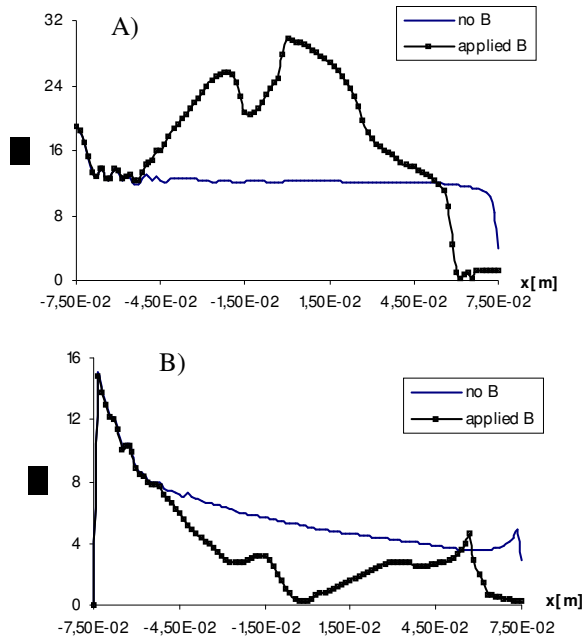


Fig. 5.7: Pressure and friction coefficient, $\beta=0$.

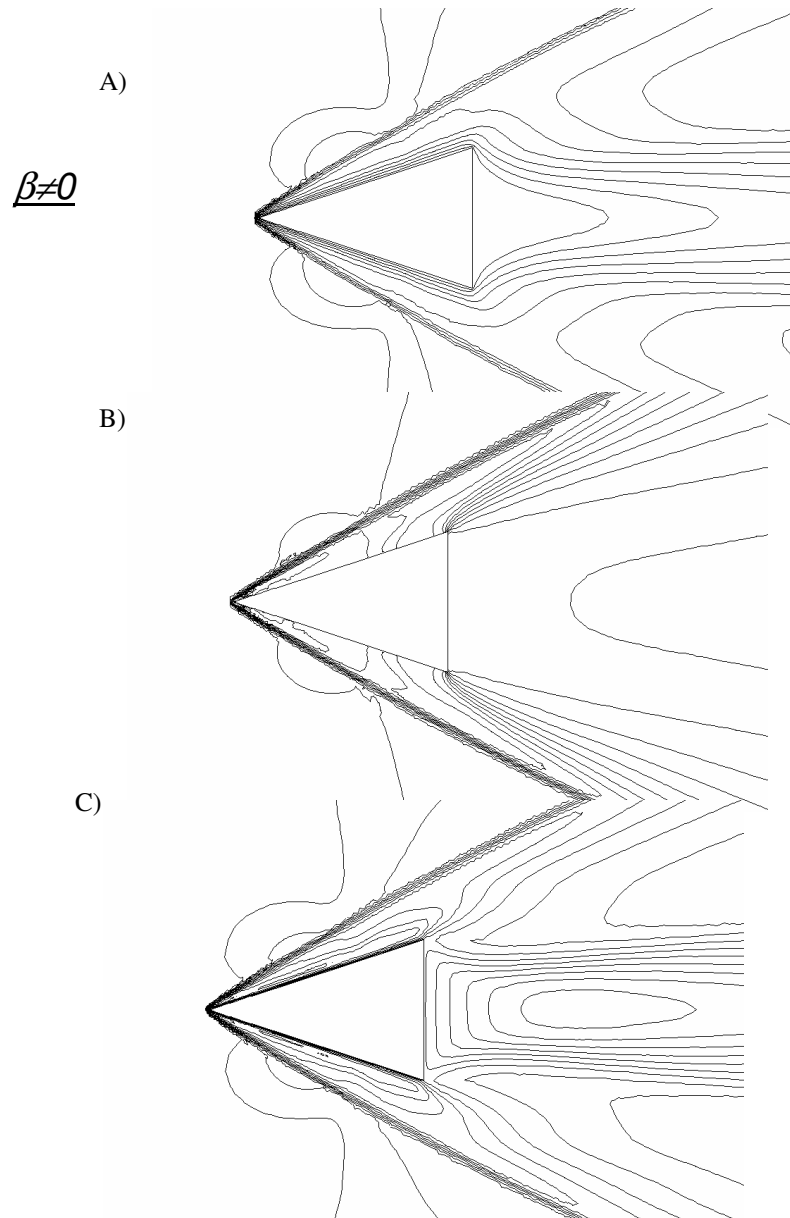


Fig. 5.8: A) *Mach isolines*, B) *Pressure isolines* C) *Temperature isolines* with $B \neq 0$, $\beta \neq 0$ and insulating walls.

The MHD interaction causes a decrease of the viscous stresses, as a consequence of the decreased flow velocity gradient. The integrals of the drag forces along the wedge sides are decreased by 36% due to the MHD interaction. The analysis has then to be performed with the inclusion of the effects of the of

the Hall parameter. Two electrical configurations have been studied. In the first configuration analysed, the current density normal to the wedge walls is set to zero. In the second configuration, the wedge walls are set to the same electric potential.

In fig. 5.8.A, 5.8.B, 5.8.C, Mach isolines, isobars and isothermals are plotted respectively, in the case of insulating wedge walls. In this case, MHD effects are drastically reduced. In the pressure and friction coefficient plot, reported in figure 5.9.A and 5.9.B it can be noted that the pressure along the wedge side weakly increases when the magnetic flux density is applied, while the friction coefficient remain largely unaffected. In this case, the variation of the integral values of normal pressure and drag force are +2% and +1% respectively.

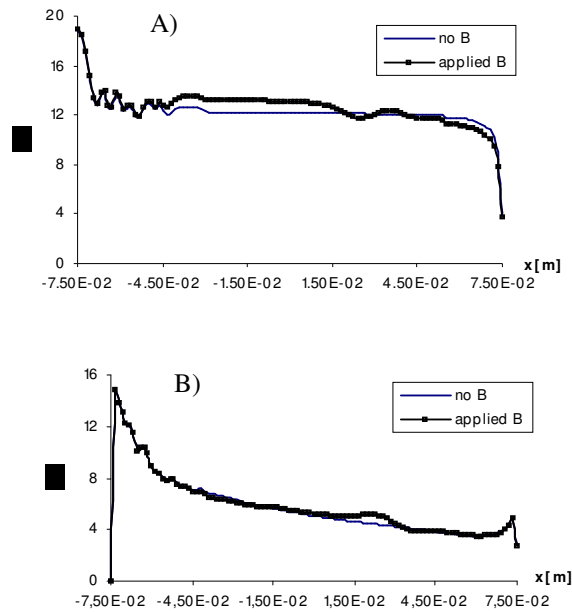


Fig. 5.7: Pressure and friction coefficient, $\beta \neq 0$.

This numerical work demonstrated that the influence of the Hall parameter is not negligible in the overall behaviour of the phenomenon. This information leads to a specific design of the blunt body used in the experimental activity, in order to optimize the MHD effect for flow control.

5.3 Experimental Activity

The knowledge of the physics of MHD-hypersonic flow interaction is essential for the application of this technology to hypersonic flight. An experimental investigation on MHD interaction at high velocities has been performed in the hypersonic wind tunnel of the TsAGI Institute near Moscow. The first results have already been published. The operating gas in this case is air¹⁸⁻²⁰. A second investigation, supported by ASI (Italian Space Agency), has been performed in Italy. The project is coordinated by the unit of Bologna and is carried out with the cooperation of several research units in Italy. The experiments are carried out in the hypersonic wind tunnel of Alta S.p.A. in Pisa. The present work will describe and discuss the first results of this project. Argon is used for this experimental investigation. This is because argon is a mono-atomic gas which is sufficiently ionized at the conditions reached in the wind tunnel.

Several diagnostic techniques have been used in this experimental work. Firstly, a map of the voltage potential has been drawn. Secondly, some information on plasma conductivity by means of V/I measurements on the blunt body electrodes was gained. Finally, optical investigation was carried out. Spectroscopy and fast gate imaging helped to understand the characteristics of the plasma in the shock region both with and without the magnetic field.

6. Plasma models.

6.1 Introduction

The determination of the atomic state distribution function (ASDF) in plasmas is crucial for a full comprehension of the phenomena involved in it. In particular, its behaviour can be analyzed when a diagnostic technique such as emission spectroscopy is used. The relation between ASDF and the underlying elementary processes is studied in the framework of a collisional radiative (CR) model.

6.2 Thermodynamic Equilibrium and its Departure

The description of a plasma that lies in thermodynamic equilibrium (TE) is rather simple: its state is fully described by relatively few quantities, such as mass density, temperature and chemical composition. Everything is ruled by statistic.

The velocity distribution is described by Maxwell, excited state distribution is described by Boltzmann, density relation between subsequent ionic states and electrons' are predicted by Saha and the behaviour of the photons is given by Plank's law. In TE, these aspects are governed by the same temperature.

It was pointed out by Oster that the distribution laws valid in TE can be derived using the principle of detailed balance (DB), and visa versa.

When the TE is no longer valid, there is a violation for DB in at least one of the relations involving plasma state (Maxwell, Boltzmann, Saha or Plank.): this leads to the substitution of detailed balance with an improper one, since production and destruction of densities are not equals.

There is a hierarchy among the type of processes which causes departure from TE. First of all, if radiation escapes from plasma, there is a violation of Plank's distribution law. However, if the overall loss of energy from escaping radiation is small when compared to the energy exchanged between material particles, Maxwell, Boltzmann and Saha are in equilibrium and the atoms, ions and electrons have the same temperature $T_m=T_H=T_e$. At this stage of equilibrium, known as local thermodynamic equilibrium (LTE), radiation has to be considered "decoupled" from matter; moreover, spatial and temporal decoupling are allowed in LTE ($\partial/\partial t \neq 0 \neq \nabla$). However, the excitation states in matter are all determined by the same temperature, defined as "excitational temperature" T^{EXC} .

A further departure from LTE is realized when different particles are subject to different forces: since the rate of energy transfer from electron e to heavy

particles M is not very efficient due to the large difference between masses m_e and M , the Maxwellization of the same species is much faster and more reliable than it is between different groups. In this situation, electrons and heavy particles are decoupled and their distribution function refers to two different temperatures. If the electron number density is large enough for comparison with neutral number density, the kinetics of electrons dominate and the ASDF is the Saha-Boltzmann function in which the temperature is the one related to electrons. This despotic behaviour of T_e must be found in the large mass ratio between e and M ($M_e/M \ll 1$).

Further TE departures can be found if the gradients become larger and the transport material significant. For example, if there is a net charge particle transport (in ionizing plasma), Saha distribution is disturbed: electrons and ions cannot recombine if they leave the active plasma region. However this does not necessarily mean that all Saha balances are going wrong. In the upper part of the atomic energy scheme, where levels are close to continuum, the ratios of ionizations and three particle recombination are effective, and the Saha balance is still valid. This situation is called electron ruled local Saha equilibrium (pLS_eE).

The lesson is that further we leave TE behind, the more the various phenomena in plasma are decoupled and the more information is needed in order to reconstruct the ASDF. Usually, as it will be shown later, the total amount of deviation is characterized by the parameter

$$b(p) = n(p)/n^s(p) \quad (6.1)$$

where the Saha density at the excited state p , $n^s(p)$ is the norm for quantifying the degree of departure of this level from equilibrium.

6.3 Improper Balances

The scenario depicted the reasons for which a deviation from equilibrium can occur. Summarizing, those reasons can be:

- A) Different forces applied to different particles
- B) Transport of radiation
- C) Transport of material particles
- D) Time dependent behaviours

If the ionization degree is high enough, the influence of the case A can be neglected. Even if B and C are present, the upper part of energy scheme can

still be in pLS_e , ruled by the Maxwellian bulk of electrons. The population of the lower excited levels is no longer ruled by Saha nor Boltzmann, but is still dominated by different improper balances. Due to hierarchy among processes and their systematic behaviour as a function of energy, it is still possible to classify those improper balances in the framework of a collisional radiative model.

A very important feature of improper balances is that they are associated with some kind of activity at a macroscopic level: in ionizing plasmas a net flow over atomic levels is created by outward diffusion of charged particles, while in recombining plasmas a net flow of deexcitation processes is related to inward diffusion of charged particles.

In figure 6.1 the possible improper balances are shown: corona balance (CB), capture radiative cascade (CRC), excitation saturation (ESB), and deexcitation saturation (DSB).

Tab. 6.1: Features of improper balances.

	Production	Destruction	Plasma properties:
CB	Excitation induced: ground state excitation	Radiative decay	Relative low n_e $b_1 \gg 1$ <i>Ionizing plasmas</i>
ESB	Excitation from lower adjacent level	Excitation to higher adjacent level	Outward transport of charged particles $b_1 \gg 1$
DSB	Deexcitation from higher adjacent level	Deexcitation to lower adjacent level	Inward transport of charged particles or irradiated plasma
CRC	Capture and cascade	Radiative decay	<i>Recombining plasmas</i> Inward transport of charged particles or irradiated plasma

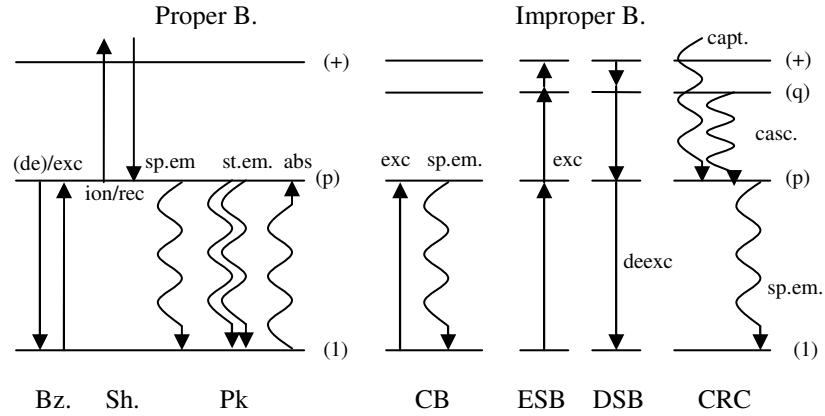


Fig. 6.1: A comparison between proper and improper balances.

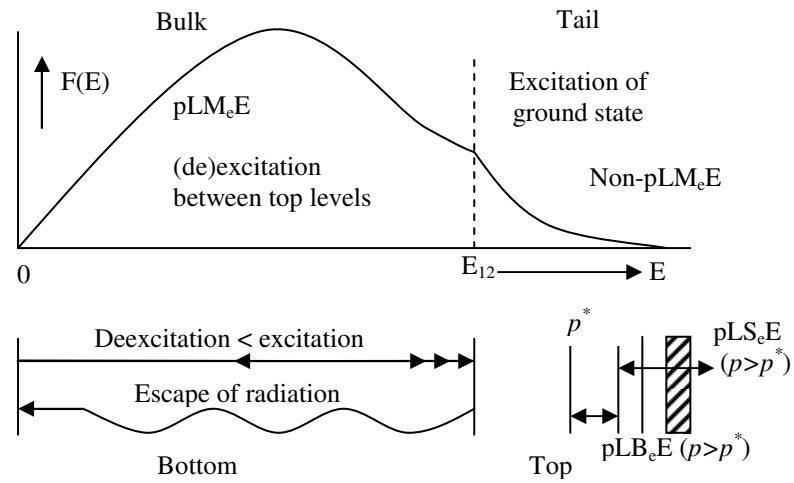


Fig. 6.2: An example of the separation in the upper and the lower energy scheme is shown. The production of excited levels must be realized by electrons with large energy ($E > E_{12}$). A low ionization degree can affect the tail of the energy distribution function of electrons violating LMeE. Also, escape of radiation affects the ASDF. The effect of this tail disturbance on Maxwell balances in the bulk is in many cases limited. In such cases we deal with a situation of pLM_eE which can sustain Saha equilibrium if p is larger than p^* .

6.4 Collisional Radiative Model

A brief description on the techniques used to calculate the *Atomic State Distribution Function* (ASDF) is given. This can be done by means of the *Collisional Radiative* model (CR). The name points to the fact that the

population of a certain level is determined by collisional and radiative processes only. If other processes like transport are neglected, it can be said that the solution of the problem can be found with a set of linear equations. This method is called quasi steady state solution (QSSS). The QSSS approach can be utilized for determining the densities of the ground state n_l and ion state n_+ , as those are inputs parameters for the set of equations. As a result, these populations can be considered as a superposition of two contributions, one coming from the ground state and the second originating from ions.

6.5 Continuity Equation

In absence of equilibrium, the density of the state p of a certain atom is determined by temporal relaxation of atomic production and destruction processes. For a plasma where electron excitation kinetic (EEK) is dominant (with a ionization degree of at least $n_e/n_a > 10^{-4}$) this reads in the following table:

Tab. 6.2: Production and destruction terms in CR models.

	PRODUCTION	DESTRUCTION
$(\partial/\partial t)n(p) + \nabla \cdot [n(p)w(p)] =$ Temporal + spatial relaxation	$\sum_{p \neq q} n_e n(q) K(q, p)$ Collisional Production	$- n(p) n_e \sum_{p \neq q} K(q, p)$ Collisional Destruction
	$+ n_e^2 n_+ K_+(p)$ Three Part. Rec.	$- n(p) n_e S(p)$ Collisional Ionization
	$+ \sum_{q > p} n(q) [A(q, p) + B(q, p) \rho_\nu]$ Cascade (Spont. + Stimulated)	$- n(p) \sum_{q > p} n(q) B(q, p) \rho_\nu$ Photo Excitation
	$+ \sum_{q < p} n(q) B(q, p) \rho_\nu$ Absorption	$- n(p) \sum_{q < p} [A(q, p) + B(q, p) \rho_\nu]$ Emission (Spont. + Stimulated)
	$+ n_e n_+ [\alpha(p) + \beta(p) \rho_\nu]$ Radiative rec. (Spont. + Stim.)	$- n(p) B(p, +) \rho_\nu$ Photo ionization

In this kind of balance, forward and corresponding backward processes are coupled:

$$(\partial / \partial t)n(p) + \nabla \cdot [n(p)w(p)] = P(p) - n(p)D(p) \quad (6.2)$$

where $P(p)$ is the production term and $D(p)$ is the destruction one.

6.6 Simplifications

Several simplifications can be taken into account for the general set of equation shown in tab 6.1.

1. Stimulated emission can be omitted, and trapping can be treated by means of an escape factor θ and its relative effective probability $\theta_p A(p, l)$. In this way, equations reduce from integrodifferential to differential.
2. Differential terms in eq. 6.2 can be neglected, as a consequence of QSSS approach.
3. Heavy particle collisions and influence of molecular transformations can be neglected if the hypothesis of an EEK plasma is sustained. In this case, transitions are related due to electron collisions or radiative decay. In this approach, it is useful to distinguish between top and bottom of the atomic system. In EEK plasma it is assumed that at least the bulk of EEDF is Maxwellian, with a tail that can be both under or over populated.
4. The overall number of levels of one species can be reduced. This leads to a reduction of the number of equation needed for solving the problem.

6.7 QSSS Solution

As explained before, the QSSS solution implies that the plasma diffusion or decay time is much longer than the lifetime of atomic states and that ground and ion states are much larger in number rather than excited states. In this way, ground and ions state can be considered as two “tanks” that can be drained or filled in a relative large time scale.

With QSSS, temporal and spatial relaxation terms are small compared to the production or destruction rates. So eq. 6.2 becomes:

$$n(p)D(p) = P(p) \quad (6.3)$$

For ground and ion state the temporal and spatial relaxations should be conserved. So the continuity equations for 1 and + are:

$$\begin{aligned}
 (\partial/\partial t)n_1 + \nabla \cdot [n_1 w_1] &= \sum_{q>1} n(q)[n_e K(q,1) + \theta_{q1} A(q,1)] + \\
 + n_e n_+ [n_e K_+(1) + \alpha(1)] - n_e n_1 \sum_{q>1} n_e K(1,q) - n_e n_1 S(1)
 \end{aligned}
 \tag{6.4}$$

$$\begin{aligned}
 (\partial/\partial t)n_+ + \nabla \cdot [n_+ w_+] &= \sum_{q>1} n(q)S(q) + n_e n_1 S(1) + \\
 - n_e n_+ \left(\sum_{q>1} n_e K(q) + \alpha(q) \right) - n_e n_+ [n_e K_+(1) + \alpha(1)]
 \end{aligned}
 \tag{6.5}$$

It is possible to give an even more compact notation to equations 6.4 and 6.5. Ground and ion level densities are input parameters for production and destruction balances. So, second term in eq. 6.3 can be considered as a sum of three terms. The first indicates the production of p level atoms directly from ion state, the second it is the production directly from ground state while the third is the p production from other levels. So it is true that:

$$n(p)D(p) = P(p) = C^+(p) + C^1(p) + C^m(p) \tag{6.6}$$

where

$$C^+(p) = n_e n_+ D_{+p} \quad D_{+p} = n_e K_+(p) + \alpha(p) \tag{6.7.a}$$

$$C^1(p) = n_1 D_{1p} \quad D_{1p} = n_e K(1, p) \tag{6.7.b}$$

$$C^m(p) = \sum_{1 \neq q \neq p} n(q) D_{qp} \quad D_{qp} = n_e K(q, p) + A(q, p) \tag{6.7.c}$$

Equation 6.9.c shows clearly the depopulation of the level q in favour of p . It is remarkable that D_{qp} has a n_e dependent (collisional) and a n_e independent (radiative) term. By convention, if $q>p$ $A(q,p)=0$.

In the same way that D_{qp} is the frequency at which the level q is depopulated, ones can introduce the frequency at which level p receives population.

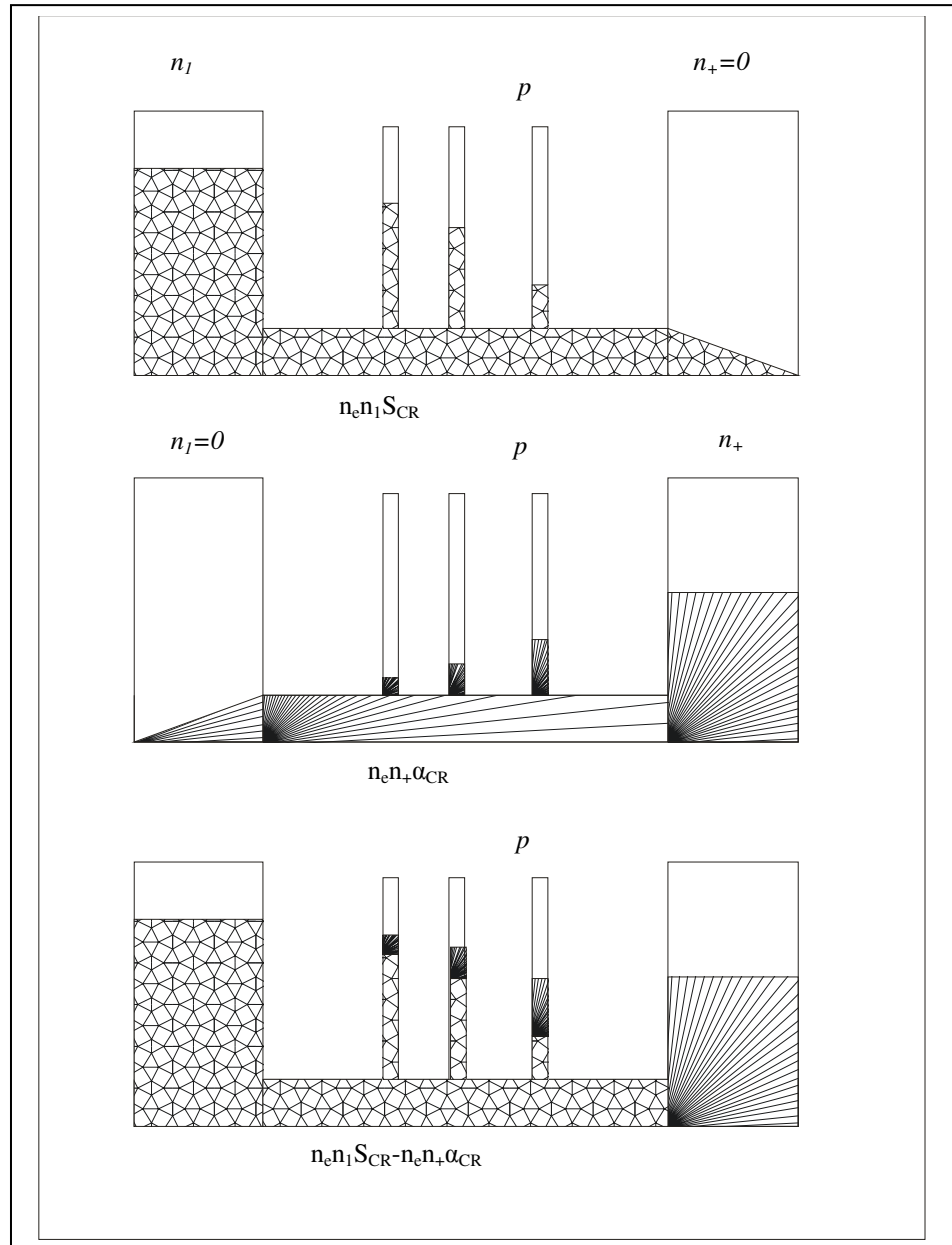


Fig 6.3: Contribution of the ground and ions density levels for the level p .

This must be related to the density of the landing level p where that level respects pLSE limit. So equilibrium production probability is defined as

$$\tilde{D}_{pq} = [n^s(q)/n^s(p)]D_{qp} = n_e K(p, q) + \tilde{A}(p, q) \quad (6.8)$$

where $n^s(q)$ and $n^s(p)$ are the densities of levels q and p when Saha distribution is respected, and the last term of the second member is defined as:

$$\tilde{A}(p, q) = n^s(p)A(p, q)n^s(q)^{-1} = A(p, q)[g(p)/g(q)]\exp(-\Delta E/kT_e) \quad (6.9)$$

The destruction factor in eq. 6.6 is given by:

$$D(p) = n_e K(p) + A(p) \quad (6.10)$$

where,

$$K(p) = \sum_{1 \neq q \neq p} K(p, q) + S(p) \quad (6.11)$$

$$A(p) = \sum_{1 \neq q < p} A(p, q) + \theta_{p1} A(p, 1) . \quad (6.12)$$

All the equations in 6.6 and 6.7 are mutually coupled by means of $C^m(p)$ contribution. But actually all the other excited states are generated from their own by the ground and excited states. Thus it must be possible to split this contribution as a function of the 1 and + levels mentioned before. So the whole system can be written in matrix representation:

$$\mathbf{HN} = \mathbf{\Pi}^+ + \mathbf{\Pi}^1 \quad (6.13)$$

in which the coupled N-1 equations (ground level excluded) are considered. Vector \mathbf{N} is a N-1 dimensional vector with the $n(p)$ values as components. The vector $\mathbf{\Pi}^+$ gives the population production coming from continuum and the equilibrium part. The components are:

$$\mathbf{\Pi}^+ = n_e n_+ D_{+p}^* . \quad (6.14)$$

The vector $\mathbf{\Pi}^1$ gives the production originating from ground levels. Here follows its components:

$$\mathbf{\Pi}^1 = n_e n_1 K(1, p) . \quad (6.15)$$

The matrix H has for $p \neq q$ components:

$$\mathbf{H}_{pq} = -D_{qp} = -n_e K(q, p) - A(q, p) \quad (6.16)$$

and

$$\mathbf{H}_{pp} = D(p) = n_e K(p) - A(p) \quad (6.17)$$

where $D(p)$ is the destruction factor of level p .

According to the principle of linear algebra, and considering true the QSSS approach, one can write

$$n(p)D(p) = P^+(p) + P^l(p) \quad (6.18)$$

which shows that the population of a certain level p can be computed by the superposition of two contributions, from ion and ground level.

In this particularly mathematical approach, $n^+(p)$ and $n^l(p)$ do not have any correlation. However in real plasmas there is a correlation between n_+ and n_l , and this leads to a relations between $n^+(p)$ and $n^l(p)$ as well. So this relation must be evaluated with a plasma model including transport phenomena.

6.8 The Distribution Function and the Relative Population Coefficients $r^+(p)$ and $r^l(p)$

Often is useful to relate the $n^+(p)$ and $n^l(p)$ contributions to the equilibrium value of the population density.

First we relate $n^+(p)$ to the Saha density and $n^l(p)$ to the Boltzmann distribution, so that:

$$n(p) = r^+(p)n^s(p) + r^l(p)n^b(p) \quad (6.19)$$

where r^+ and r^l are the so called population coefficients.

These coefficients are defined as follows:

$$\begin{aligned} r^+(p) &= n^+(p)/n^s(p), \\ r^l(p) &= n^l(p)/n^b(p) \end{aligned} \quad (6.20)$$

In this notation, both ground and ion levels are treated as reservoirs in an equivalent way. However, there are large differences between those two fundamental states. Differently from ion state, ground one is separated from other levels by a large energy gap. Since it is clear that ions will contribute more broadly to the formation of p level, a notation that points this fact seems to be more convenient. This can be realized dividing 6.19 by $n^s(p)$:

$$b(p) = r^+(p) + r^1(p)b_1. \quad (6.21)$$

This expresses the deviation from the equilibrium $b(p)=n(p)/n^s(p)$ of the p level as a linear function of the departure of the ground level b_1 .

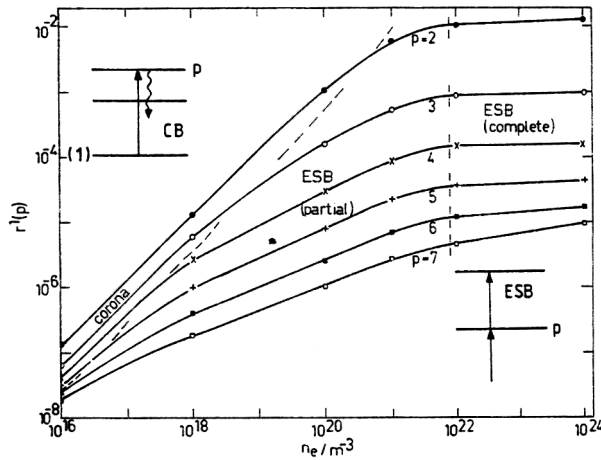


Fig. 6.4: $r^1(p)$ coefficient for an optically thin hydrogen plasma as a function of n_e for $T_e=3.2*10^4$ K. Note the loss of linearity due to the transition from CB to ESB process.

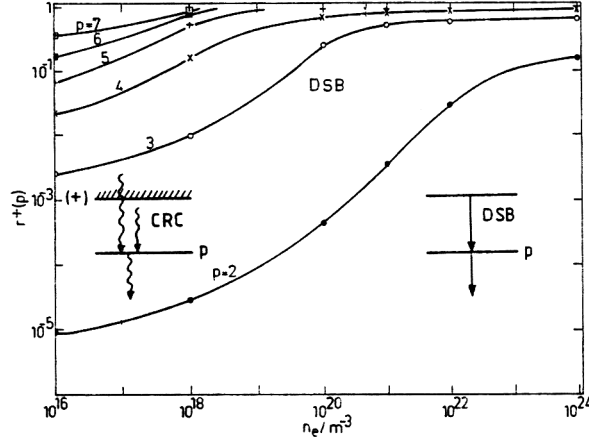


Fig. 6.5: $r^+(p)$ coefficient for an optically thin hydrogen plasma as a function of n_e for $T_e=3.2 \cdot 10^4$ K. Note the n_e loss of dependence in transitions between CRC and DSB.

6.9 Coefficient for Total Ionization and Recombination

So it is possible to give the compact notation for the equations 6.4 and 6.5:

$$\begin{aligned} (\partial/\partial t)n_1 + \nabla \cdot [n_1 w_1] &= n_e n_+ \alpha_{CR} - n_e n_1 S_{CR} \\ (\partial/\partial t)n_+ + \nabla \cdot [n_+ w_+] &= -n_e n_+ \alpha_{CR} + n_e n_1 S_{CR} \end{aligned}$$

where α_{CR} and S_{CR} are respectively the coefficients for total recombination and ionization. Combining those latter equations with 6.20 it can be found that

$$\begin{aligned} S_{CR} &= S(1) + \sum r^l(q) [n^s(q)/n^s(1)] S(q) \\ \alpha_{CR} &= n_e K_+(1) + \alpha(1) + \sum [n_e K_+(q) + \alpha(q)] - n_+^{-1} \sum r^+(q) S(q) n^s(q) \end{aligned} \quad (6.21)$$

Here it is shown that the recombination is coupled with the r^+ coefficient, while the total ionization is related to the r^l coefficient. It is clear that a pure radiative system, where $n_e \rightarrow 0$ will be dominated by r^+ while in a purely collisional system ($n_e \rightarrow \infty$) the factor leading will be r^l .

6.10 The Boundary properties

The common depopulation factor will mainly generate the common properties of r^l and r^+

$$D(p) = n_e K(p) + A(p) . \quad (6.22)$$

The depopulation factor is related to the competition between free and bounded electrons: the first term determines the boundary in the collisional/radiative model, while the second is inherent to various Boltzmann factors in $K(p)$. Here we introduce two parameters to justify such a competition:

$$\tilde{N}_e(p) = n_e K(p) / A(p) \quad (6.23)$$

$$\tilde{T}_e(p) = kT_e \delta / |E_p| = \delta / \varepsilon_p \quad (6.24)$$

in which δ is an adjustable parameter. The first one gives an indication of the number of collisions per radiative life time. It can be said that

-The level is collisional for $\tilde{N}_e(p) > 1$

-The level is radiative for $\tilde{N}_e(p) < 1$

The second parameter (6.24) is related to the overall kinetic energy of the mean free electrons relative to that of the bound electrons at the level p . It is said that

-The level is hot if $\tilde{T}_e(p) > 1$

-The level is cold if $\tilde{T}_e(p) < 1$

For low n_e values, the parameter of equation 6.23 makes a splitting in the energy scheme. Lower levels are dominated by radiation, while uppers are collisional. The principal quantum number (pqn) at which this splitting can be notated, can be computed by means of:

$$\tilde{N}_e(p) = 1 = n_e K(p_{CR}) / A(p_{CR}) \quad (6.25)$$

and this leads to

$$N_e^* p_{CR}^9 = 1.32 \times 10^{23} \frac{T_e^* + 2}{T_e^{*0.5}} \cdot \frac{3 \ln p_{CR} - \zeta}{\ln(2/\varepsilon_{p_{CR}} + 1.3)(1 + \varepsilon_{p_{CR}}/4)} \approx 9 \times 10^{23} \quad (6.26)$$

Clearly for a given p the critical electron number density $n_e^c(p)$ at which that level is collisional dominated can be found.

Moreover, for low T_e values, it can be found that the energy scheme is split in a cold and a hot part. The principal quantum number of such a splitting is given by:

$$p_{hc} = Z \sqrt{R/(kT_e \delta)}. \quad (6.27)$$

For a given p this equation gives a critical temperature $T_e^C(p)$ in such a way that for all the temperatures $T_e > T_e^C(p)$, all the levels $q > p$ are collisional hot. The collisional hot to cold level, sometimes is called bottleneck. Levels above this neck are ruled by ion state, while levels under are determined by ground state.

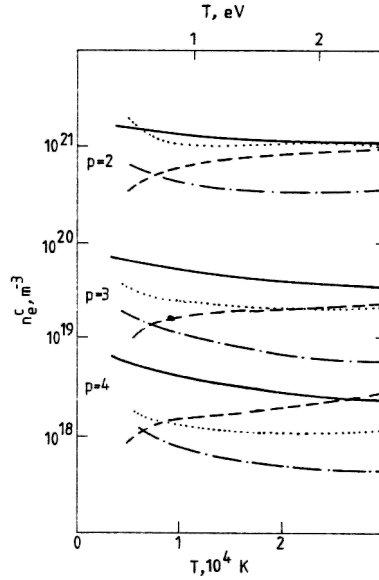


Fig. 6.6: The critical densities for hydrogen levels $p=2, 3, 4$ as a function of T_e .

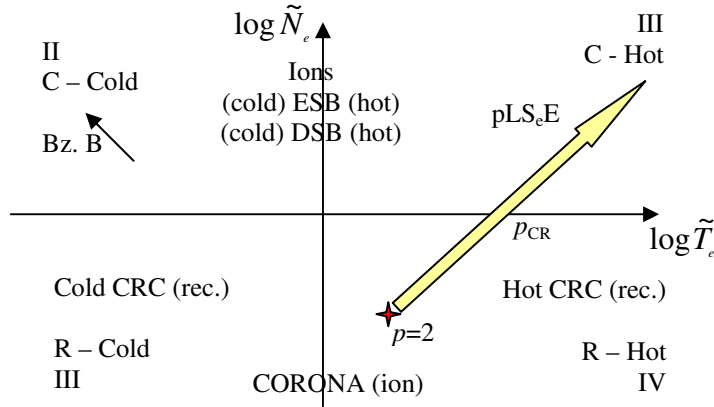


Fig. 6.7: The domain plane. Upper half is the collisional, while lower half plane concern radiative levels. The line starting from the star ($p=2$) is a domain curve, the projection of an ASDF.

6.11 The Domain Plane

Since the parameters \tilde{N}_e and \tilde{T}_e are so meaningful in describing plasma conditions we can plot a 2D graph with those quantities.

The vertical axis is the $\log \tilde{N}_e$, while the horizontal one is the $\log \tilde{T}_e$.

Each of the six balances, two proper (Saha and Boltzmann) and four improper (ESB, DSB, CB, and CDC) has an area in this plane:

- I) In the first quadrant there are the collisional hot levels. The definitions of \tilde{N}_e and \tilde{T}_e show that, for increasing p values, this first quadrant will be reached. So that the top of any system has to reach this quadrant. Here there are the ESB (DSB) and Saha balance.
- II) In the second quadrant there are the collisionally cold levels. These levels are frequent in interactions with cold electrons and deexcitation will be dominant. The balances are the ESB, DSB. The particular case of an ionizing system leads to a Boltzmann balance here.
- III) In the third quadrant we find radiative cold levels. There are the CRC-cold for recombining plasmas and the CB for ionizing.
- IV) Conversely, in the fourth quadrant we find the radiative hot levels. Here there are hot CRC and the CB.

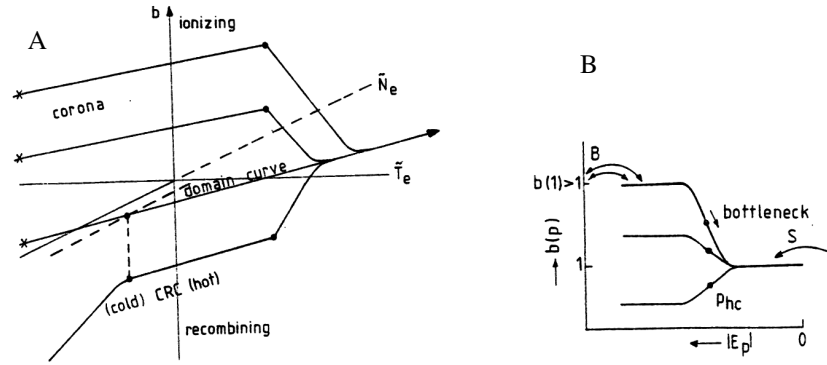


Fig. 6.8: In A it is shown a family of ASDF (case A) having the same domain curve. Differences between ASDF are generated by different b_1 values. In B it is the same, but with case B properties.

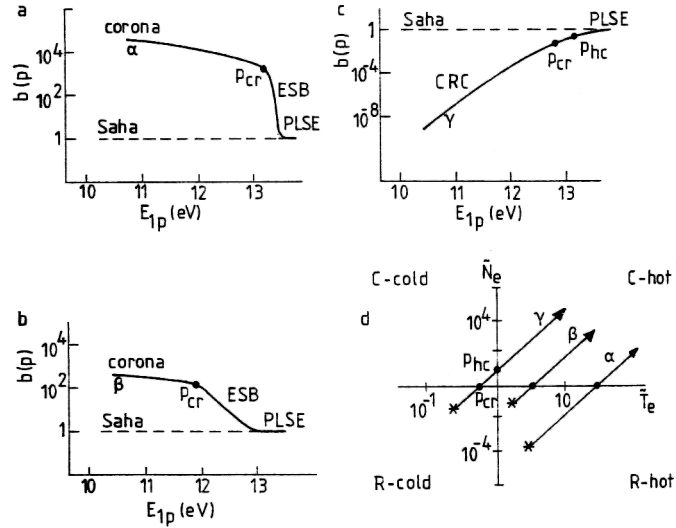


Fig. 6.9: Distribution functions and domain curves. In (a) an optically thin H plasma with $n_1=10^{19} \text{ m}^{-3}$, $n_e=10^{18} \text{ m}^{-3}$ and $T_e=3.2 \cdot 10^5 \text{ K}$. (b) an optically thin H plasma with $n_1=10^{18} \text{ m}^{-3}$, $n_e=10^{20} \text{ m}^{-3}$ and $T_e=3.2 \cdot 10^5 \text{ K}$. (c) an optically thin H plasma with $b_1=0$, $n_e=10^{18} \text{ m}^{-3}$ and $T_e=2 \cdot 10^3 \text{ K}$. (d) domain curves for a, b and c.

7. Recombining system

7.1 Capture Radiative Cascade (CRC) Balance

Quadrants IV and III of figure 6.7 are dominated by the purely radiative capture cascade (CRC) balance. Those models were presented by astrophysicists like Baker and Menzel.

In the QSS there must be a balance between capture and radiative cascade on one side, and radiative decay on the other: so the production / destruction balance of a certain level in CRC should be:

$$n(p) \sum_{l < p} \theta_{pl} A(p, l) = n_e n_+ \alpha(p) + \sum_{u > p} n(u) A(p, l). \quad (7.1)$$

Since there is a difference between radiatively hot ($\epsilon_p = |E_p| / kT < 1$) and R-cold levels, it is useful to distinguish between the two cases of hot CRC (IV quadrant) and cold CRC (III quadrant).

7.2 The Hot CRC (IV)

In this quadrant, the total number of decay processes at the level p can be written as:

$$\begin{aligned} n(p) A(p) &= [n(p) / G^A(p)] \Gamma \ln L_p / E_{p-1,p} = \\ &= n(p) \gamma Z^4 p^{-5} (3 \ln p - \zeta) \end{aligned} \quad (7.2)$$

in which L_p is the largest decay gap:

$$\begin{aligned} L_p^A &= c_p^A E_{1p}, \quad \zeta = 0.25 \approx \ln(2/c^A), & \text{Case A} \\ L_p^B &= c_p^B E_{2p}, \quad \zeta = 1.84 \approx \ln(8/c^B), & \text{Case B} \end{aligned}$$

it is possible to put the cascade and capture contribution in one formula as follows:

$$n_e n_+ \alpha(p) + \sum_{u > p} n^S(u) A(u, p) = n^S(p) \tilde{\alpha}^S(p) \quad (7.3)$$

with

$$\begin{aligned}\tilde{\alpha}^*(p) &= \gamma Z^4 p^{-5} [3 \ln p - \xi(T_e)] \\ \xi(T_e) &\cong \ln(R/kT_e) + 0.8\end{aligned}$$

With the assumption that the actual value of the cascade contribution is not far removed from its equilibrium value, we obtain:

$$b(p) = \frac{3 \ln p - \xi(T_e)}{3 \ln p - \zeta}. \quad (7.4)$$

The corresponding value of overpopulation is equal to:

$$\delta b(p) = b(p) - 1 = \frac{\zeta - \xi(T_e)}{3 \ln p - \zeta} = \frac{\ln(c'kT_e/L)}{\ln(L/E_{p-1,p})}. \quad (7.5)$$

A more general case is extended to $n_e \rightarrow 0$, where the limit reads:

$$\delta b(p) = \sum \frac{\delta b(p) \tilde{A}(p,q)}{A(p)} + \frac{\zeta - \xi(T_e)}{3 \ln p - \zeta}. \quad (7.6)$$

The difference between equations 7.5 and 7.6 is evident: it reflects the departure from pLSE of the higher levels, so that the first term of the second member of equation 7.6 can not be neglected anymore.

However, in the worst case, cascade can affect ASDF less than 30% whereas the rest (due to capture) retains its equilibrium function as long as EEDF is Maxwellian.

From equation 7.5, the consequent phenomena can be predicted:

- I) For low temperatures the equilibrium departure for opacity case A is more severe than for B. In fact, $L^B < L^A$.
- II) In the limit $p \rightarrow \infty$ we have $\delta b \rightarrow 0$. So Saha density is established without the presence of a Saha balance.
- III) The equilibrium departure of δb is a weak function of p
- IV) The sign of $\zeta - \xi$ is determined by the electron temperature and its relation to the largest decay gap.

It should be considered that the temperature dependence of equation 7.3 is the result of the T_e dependence of capture only. But capture is the main production term in CRC domain, so the cascade temperature is a second order effect. This treatment of CRC is based on the fact that ASDF depends only on the principal quantum number, and the various orbitals are statistically populated.

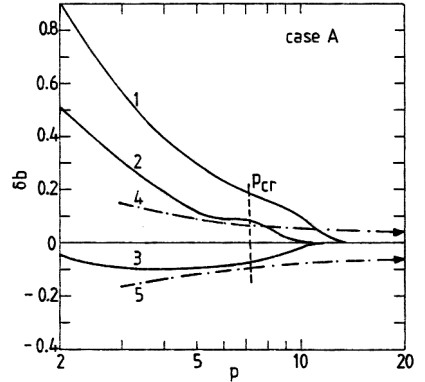


Fig. 7.1: Relative overpopulation as a function of p for different temperatures: (1) $T_e=10^6$ K (2) $T_e=5*10^5$ K (3) $T_e=2*10^5$ K, for $n_e=10^{16} m^{-3}$ (4) $T_e=3.2*10^5$ K (5) $T_e=1.6*10^5$ K with $n_e=0$. Collisional/radiative boundary is for $n_e=10^{16} m^{-3}$ and indicate with p_{cr} .

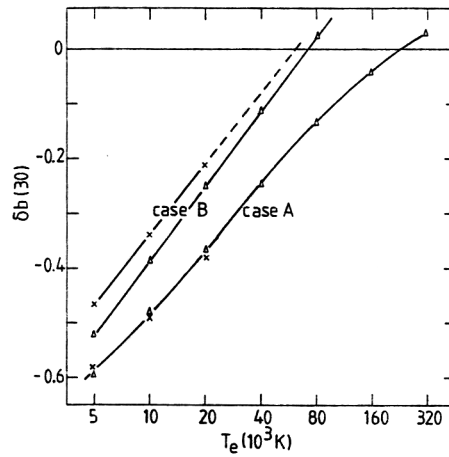


Fig. 7.2: Relative overpopulation of level $p=30$ as a function of electron temperature.

7.3 The Cold CRC

When small T_e and large ε_p occur in the III quadrant can describe the plasma behaviour.

In this domain the capture rate is much smaller than the equilibrium amount of decay processes, so we can expect very large deviations from the pLSE density. Therefore, the quasi-pLSE approach is not valid in this domain.

A valid method for gaining information on the main features of the distribution function can be to neglect the cascade contribution and retain capture as the only population process.

The following approximation can be found:

$$n_e n_+ \alpha(p) = [n^s(p) \Gamma / G^a(p)] \exp(-\varepsilon_p) / \varepsilon_p \quad (7.7)$$

Combining this with precedent equations, one can find

$$n(p)(3 \ln p - \zeta) = n^s(p) \exp(-\varepsilon_p) / \varepsilon_p \quad (7.8)$$

but with

$$\begin{aligned} \varepsilon_p &= Z^2 R / (p^2 k T_e) \\ (3 \ln p - \zeta) &\cong 2\sqrt{p} \end{aligned} \quad (7.9)$$

we finally obtain:

$$b(p) \exp / \varepsilon_p = p^{1.5} k T_e / 2 Z^2 R \quad (7.10)$$

From the figure 7.3 one can deduce that the population density per statistical weight is an increasing function of p , which means that there is an inversion in density within the system.

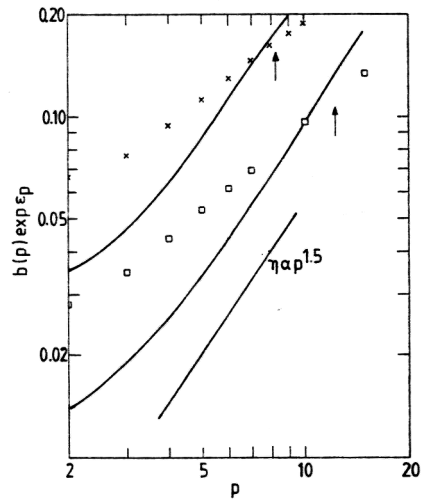


Fig. 7.3: $b(p)\exp \varepsilon_p$ as a function of the pqn . Crosses indicate a pure CRC ($n_e=0$) with $T_e=2.5 \cdot 10^3$ K. Squares $n_e=10^{10} \text{ m}^{-3}$, $T_e=10^3$ K.

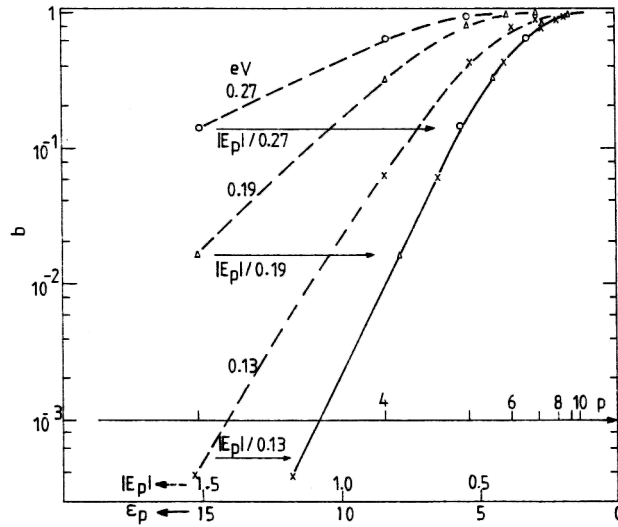


Fig. 7.4: Experimental results in DSB domain. Log b versus E_p . Arrows indicate the normalization with $\varepsilon_p = E_p/kT_e$.

7.4 Cold Deexcitation Saturation Balance (DSB)

In the second quadrant there is the DSB. Due to $\tilde{N}_e > 1$, e-induced transitions occur more than once per radiative lifetime. But these are cold transitions (since $\tilde{T}_e < 1$) so deexcitation prevails over excitation.

The distribution function under such a process can be approximated by:

$$b(p) \approx (\varepsilon_p^3 / 3! + \varepsilon_p^2 / 2! + \varepsilon_p + 1) \exp(-\varepsilon_p) \approx 0.75 \varepsilon_p^{3/2} \exp(-\varepsilon_p) \quad (7.11)$$

In the domain of cold DSB, The distribution function can be expressed solely in terms of ε : consequently, when $\varepsilon \gg 1$, it largely deviates from Saha equilibrium.

7.5 Hot Deexcitation Saturation Balance (DSB)

In quadrant I it is possible to find levels dominated by hot collisions, in which the free electrons are the leading particles since $\tilde{T}_e > 1$. This means that excitation will be stepwise rather than jumpwise.

Stepwise behaviour is essential for quadrant I. If it is present, it is possible to define an excitation flow j and to construct a continuity equation for the excitation space which describes how this flow changes in its course through this one.

These changes are functions of sources and sinks. The ionizations I and the radiative decay D are sinks, while capture cascade CC and three particles recombination R are sources. By means of the continuity equation, one can say that:

$$\text{div}(j) = R + CC - I - D \quad (7.12)$$

the divergence of the net flow is related to sinks and sources. Flows, sinks and sources are related to the population density. If the boundary conditions are known, the distribution function can be determined.

Without giving too many details that can be found in literature, one can classify parts and shapes of the distribution function as predicted by a differential equation which shows a competition between radiative and collisional processes. For a value of $\tilde{N}_e \ll 1$ the solution following

$$\delta b = (\zeta - \xi) / (3 \ln p - \xi) \quad (7.13)$$

is exactly the same as for the CRC in pLSE condition. This is not surprising, since $\tilde{N}_e \ll 1$ is in the CRC domain. For values belonging in an area where $\tilde{N}_e \gg 1$ we get the solution (out from the situation of pLSE where $\delta b=0$)

$$\delta b = -b_0 p^{-x}. \quad (7.14)$$

The value of b_0 is determined by the boundary condition of the low side of p. The factor x should be equal to

$$x = 2.5(1 - \sqrt{1 + 0.16s/k}). \quad (7.15)$$

It is important to notice that the exponent of p is dependant only on the s/k ratio, the so called ‘‘competition parameter’’ depending on the ratio ψ_s / ψ_k .

7.6 The boundary Between CRC and Hot DSB

The equilibrium departures, present in quadrant IV and propagating to quadrant I are due to radiative decay processes. As a function of effective decay probability $A_{eff}(p)$, this equilibrium deviation can create both an underpopulation and an overpopulation, depending on $T_e^* = T_e Z^2$.

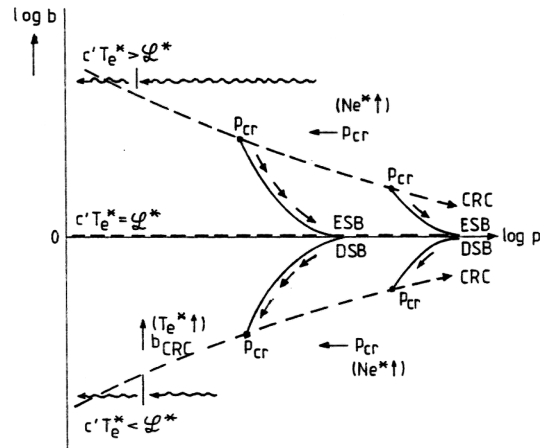


Fig 7.5: A sketch of nested ASDFs' for different values of N_e^* and T_e^* . The low P (CRC) branch –dashed– of each ASDF is determined by T_e^* and sets the

boundary to the high p (D/ESB) branch –solid-. The position of p_{cr} is mainly determined by N_e^* . The arrows along curves indicate the (de)excitation flow preparing the advent of pLSE.

If $c T_e^*$ is smaller than the reduced largest decay gap $L=LZ^2$, then the capture and cascade stay well behind the equilibrium value of decay processes which result in an underpopulation. Conversely, if $c T_e^* > L$ the system is led to an overpopulation. In both cases, over or underpopulation has to be removed with collisional processes, that is a precursor of pLTE.

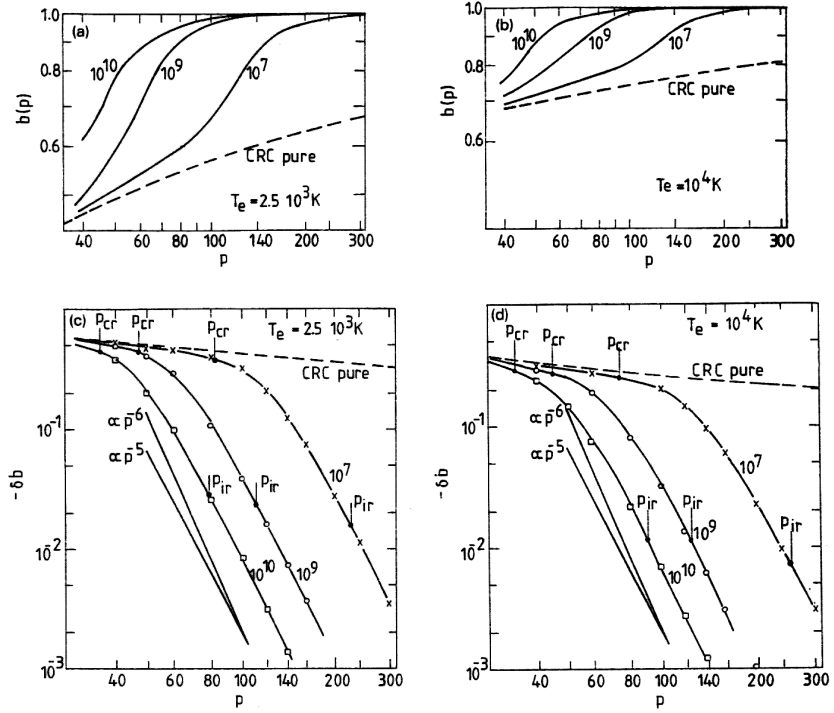


Fig. 7.6: The b factor in an hydrogen plasma as a function of pqn for two different temperatures T_e and three different n_e .

8. Experimental Set Up

8.1 High Enthalpy Wind Tunnel

Alta-CPR High-Enthalpy Arc-heated Tunnel (HEAT) is a pulsed hypersonic wind tunnel operative since 1996^{21,22}. It can produce Mach 6 flows in a low to medium Reynolds number range (10^4 - 10^6). In the wind tunnel settling chamber the gas is heated by means of an arc discharge powered by a 260 kW DC power supply and delivering arc currents up to 630 A during running times of 20-300 ms. In the settling chamber a total specific enthalpy up to 6 MJ/kg with stagnation pressures up to 9 bar can be obtained. The gas heater can be operated with air, nitrogen, argon, CO₂ in a pulsed, quasi-steady mode. At the exit of the settling chamber a nozzle is mounted. The effective test section at the exit of the nozzle has a diameter of 55 mm. The arc heater scheme is shown in figure 8.1. The nozzle is shown in figure 8.2.

The wind tunnel (gas heater and nozzle) is installed on a vacuum test section of 600 mm diameter. In the test section there are optical accesses from all sides. This section is connected to a vacuum chamber of a volume of 4.1 m³. The chamber is evacuated by four rotary pumps to reach an ultimate pressure of 10 Pa before each run. Up to 100 test runs can be carried out per day. The flow characteristics are obtained by means of pitot probes²³ provided with fast miniaturized piezo-resistive pressure transducers, and stagnation temperature probes, provided with fast coaxial thermocouples or thin-film gauges. In the settling chamber the pressure is measured by fast pressure transducers. From all pressure signals accuracies of about 3% are obtained. The total enthalpy is estimated from the arc discharge power and compared with the values obtained from the stagnation temperature measured in the test section. The total enthalpy error is ± 5 -10%.

For the present activity the test gas is argon (Ar). A short Mach 6 conical nozzle with an effective exit test section of a diameter of about 50 mm is used. A series of ignition tests allowed for the identification of the best conditions for the arc discharge. The arc voltage drop is below 100 V for all test conditions. Three typical test conditions are identified with a total pressure ranging between 0.6 and 1 bar (see Tab. 8.1). Pressure fluctuations are observed at low pressure levels. This is due to the turbulent conditions created in the settling chamber. The flow is steady for pressure levels greater than or equal to 0.6 bar.

The gas properties at the nozzle exit for the three test conditions are summarized in Table 8.1. The values shown in the table are calculated by means of the one dimensional nozzle theory, the assumption of isentropic flow.

Table 8.1. Flow characteristics at the nozzle exit for the three chosen test conditions.

Condition	I_{arc} [A]	V_{arc} [V]	M	P_{tot} [bar]	H_{tot} [MJ/kg]	T_{tot} [K]	m_{dot} [g/s]
1	618	76	5.72	1.02	1.41	2713	14
2	613	68	5.70	0.85	1.81	3483	9
3	610	60	5.68	0.65	2.10	4041	7

Condition	p_{exit} [mbar]	T_{exit} [K]	ρ_{exit} [kg m ⁻³]	n_{Ar} [m ⁻³]	u [m/s]
1	2.12	229	$4.44 \cdot 10^{-3}$	$6.64 \cdot 10^{22}$	1607
2	1.77	294	$2.88 \cdot 10^{-3}$	$4.31 \cdot 10^{22}$	1820
3	1.35	341	$1.90 \cdot 10^{-3}$	$2.84 \cdot 10^{22}$	1960

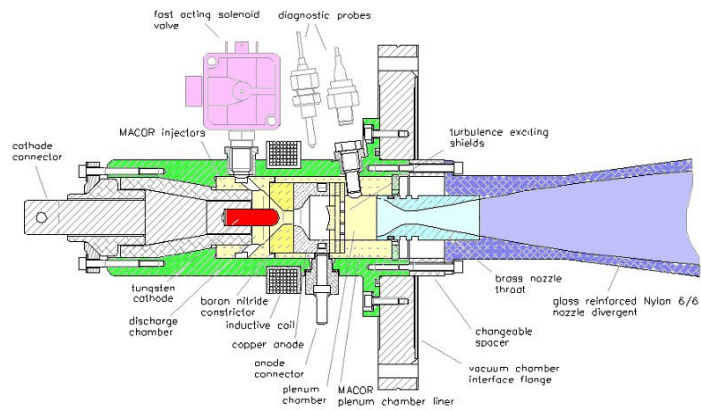


Fig 8.1: Arc heater scheme.



Fig. 8.2: Nozzle mounted at the exit of the settling chamber.

8.2 Magnetic Field

The design of the magnetic field was one of the most crucial tasks of the experiment. Conjointly with the test case electrode design, it has been decided that a normal to flow magnetic field would be the best option.

Permanent magnets were not considered useful, mostly for their temperature-sensitive behaviour.

So the design of a C shaped iron core was developed, with a copper winding useful to provide the necessary amps for turns for the B field.

In order to power supply the inductor, a pulse forming network (PFN) was utilized. This PFN is a parallel/series R L C network capable of a 5ms square shape current pulse with a maximum value of 4kA: this current was used for supplying an electromagnet, useful also as a support for the test case placed between its polar expansion, in an integrated design.

The electromagnet proportions were determined in proportions by means of a magnetostatic FEM code, in conjunction with a model of the whole system (PFN plus magnet modelled as an RL//C network) for the dynamic behaviour over time. The last model was also precious for determining the ballast resistor of the PFN discharge, necessary to prevent dangerous sign-inversions of the current.

The final design was a C shaped inductor (figure 8.3) of pure iron, with a 100mm X 100mm square solid core. All around the inductor, a 65 turn copper winding, plugged with the PFN network, sustains the B-field.

The test case has been fixed by means of two aluminium fins between the polar expansions of the magnet, close to the symmetry plane.

The B field was then measured in the final set-up by means of some arrays of B-derivative probes, placed in the air gap of the magnet. B field values are visible in table 8.2.

the B-Field is changing over time. For a very narrow time window of 2-3 hundreds of microseconds around the maximum value it can be considered as a constant.

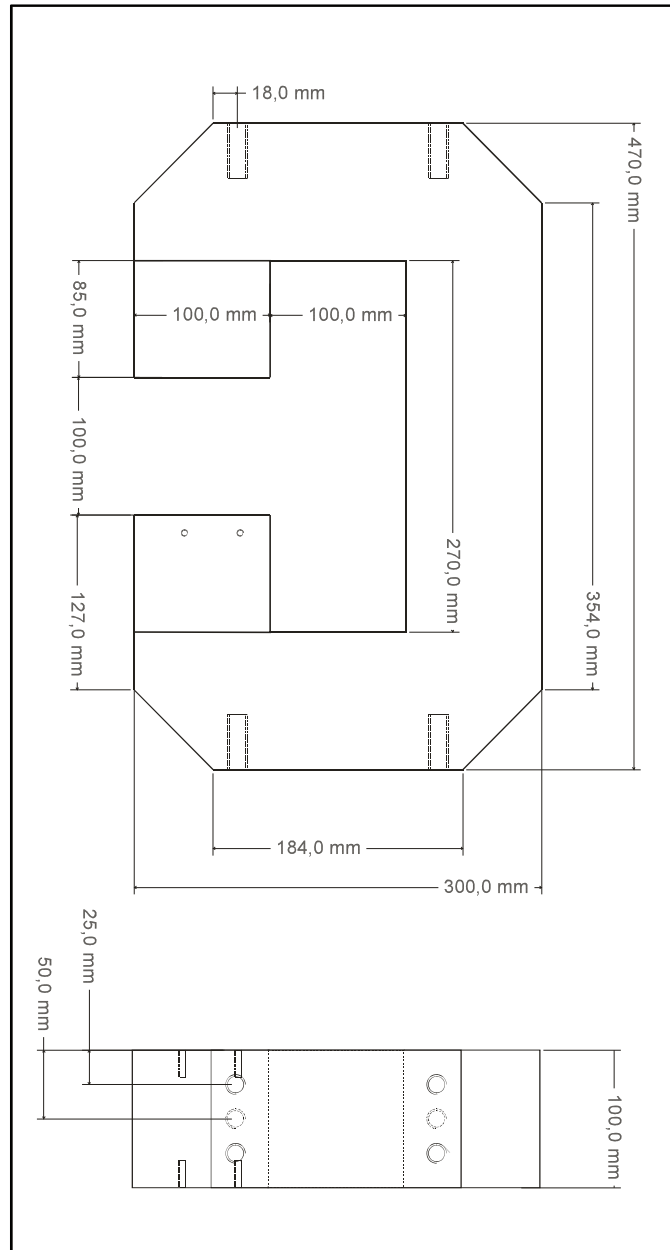


Fig. 8.3: Magnet Design.

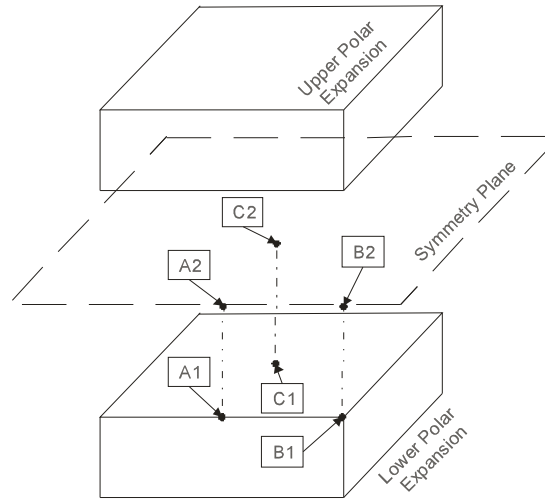


Fig. 8.4: Magnetic field probes position.

Table 8.1: B-field maximum value in the air gap.

	PFN charge 1000V	PFN charge 1400V
A1	0.437 [T]	0.534 [T]
B1	0.519 [T]	0.655 [T]
C1	0.326 [T]	0.43 [T]
A2	0.22 [T]	0.286 [T]
B2	0.185 [T]	0.24 [T]
C2	0.255 [T]	0.34 [T]

8.3 Hall electrodes configuration

A crucial point, which has to be taken into account when designing an experiment on MHD interaction in low pressure plasmas, is the high value assumed by the Hall parameter, due to the reduced collision rate between electrons and heavy particles. In a two dimensional geometry, assuming a reference system (shown in figure 8.5), where the gas velocity \mathbf{u} and the magnetic flux density \mathbf{B} lie on the x-y plane, while electromotive force $\mathbf{u} \times \mathbf{B}$ is directed along the z-axis, the generalized Ohm's law is:

$$\mathbf{J} = \sigma (\mathbf{E} + \mathbf{u} \times \mathbf{B}) \quad (8.1)$$

where the conductivity tensor, in the coordinate system considered, has the following expression:

$$\boldsymbol{\sigma} = \frac{\sigma}{1 + \beta_e^2} \begin{bmatrix} 1 + \beta_x^2 & \beta_x \beta_y & \beta_y \\ \beta_x \beta_y & 1 + \beta_y^2 & -\beta_x \\ -\beta_y & \beta_x & 1 \end{bmatrix} \quad (8.2)$$

and:

$$\beta_x = B_x \frac{\beta_e}{B} = \mu_e B_x, \quad (8.4)$$

$$\beta_y = B_y \frac{\beta_e}{B} = \mu_e B_y.$$

Assuming then a velocity \mathbf{u} in the x direction, and a \mathbf{B} field in the y direction, and that the Faraday component of the electric field E_z is equal to 0, Ohm's law yields:

$$j_x = \frac{\sigma}{1 + \beta_e^2} (E_x + \beta_e u B)$$

$$j_y = \sigma E_y$$

$$j_z = \frac{\sigma}{1 + \beta_e^2} (-\beta_e E_x + u B) \quad (8.5)$$

As a matter of fact, a Hall parameter higher than unity can easily impair the MHD interaction, as the conductivity is approximately reduced by a β_e^2 factor. In order to maximize the current density J_z and, consequently, the MHD body force, the current density J_x should be set equal to zero, thus obtaining the maximum Hall field :

$$j_x = \frac{\sigma}{1 + \beta_e^2} (E_x + \beta_e u B) = 0 \Rightarrow E_x = -\beta_e u B$$

$$\Rightarrow j_z = \frac{\sigma}{1 + \beta_e^2} [-\beta_e (-\beta_e u B) + u B] = \sigma u B \quad (8.6)$$

Thus, it is possible, in principle, to obtain an adequate MHD interaction even in plasmas with a high Hall parameter.

In figure 8.5 a schematic of the test body is shown. The test body is a Macor ramp with a flat surface where eight copper electrodes are buried flush with it. The z-direction (see figure 8.5) is perpendicular to the flow direction. The x-direction forms an angle (ramp angle θ) of 12.5° with the flow direction. Sets of probes are placed on the test body surface, at the inlet and at the outlet of it, and between adjacent electrodes. In the y-direction a magnetic field is generated by the iron core magnet (figure 8.6).

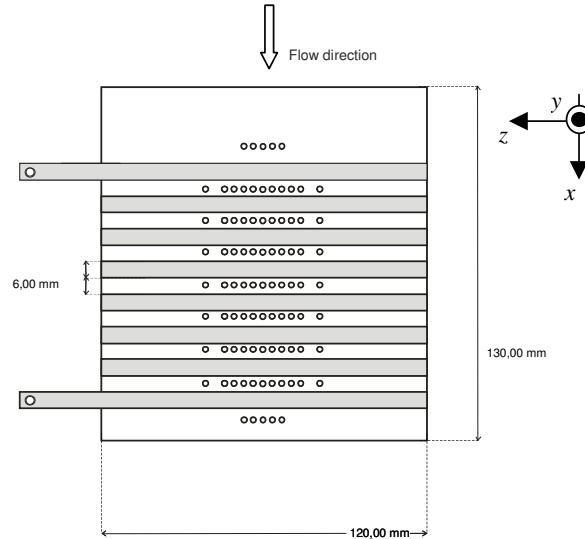


Fig 8.5: Schematic of the test body.

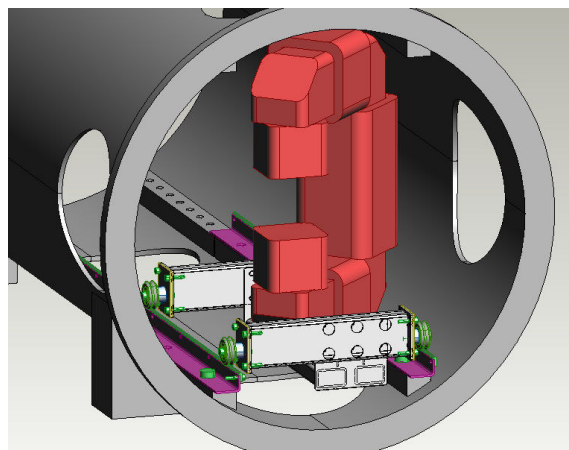


Fig. 8.6: Magnet view in the vacuum section.

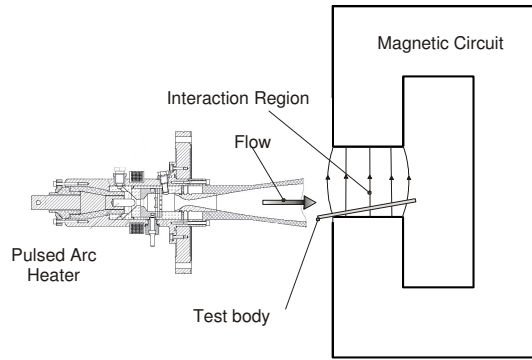


Fig. 8.7: Layout of the experiment.

8.4 Shock Layer on the Test Body Surface

The shock region in front of the test body is sketched in figure 8.8. An image of the shock for condition 2 ($p_{\text{tot}} = 0.85$ bar) is shown in figure 8.9. The image is taken by means of the fast shutter CCD camera. The velocity u_{sh} inside the shock layer is assumed to be parallel to the wedge plane (surface of the ramp). Thus the angle between u_{sh} and the free stream velocity direction is given by the ramp angle θ . The ideal theory of oblique shock²⁸ allows to calculate the flow conditions in the shock layer. As the ramp angle θ is 12.5° , the shock angle β is calculated to be 22° . The calculated value of the Mach number in the shock layer (M_{sh}) for the three test conditions is 3.56. The calculated pressure, temperature, mass density, number density and flow velocity of the gas within the shock layer are listed in Tab. 8.3.

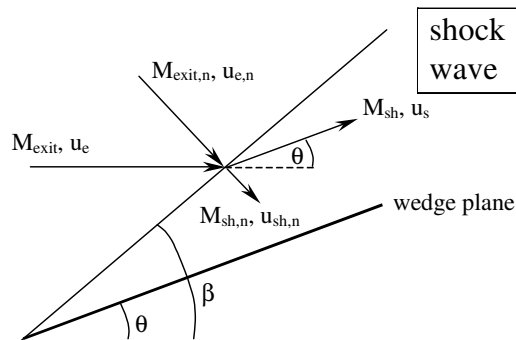


Fig. 8.8: The oblique shock wave on the ramp surface.

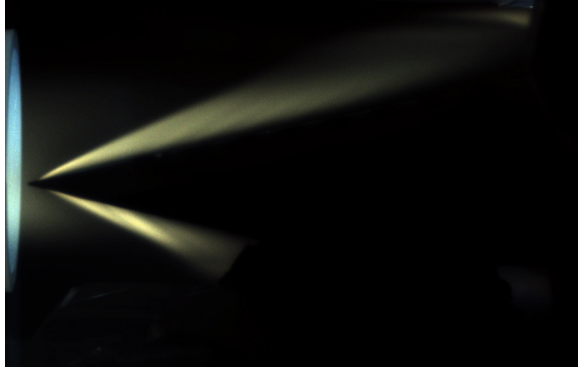


Fig. 8.9: Fast shutter CCD camera image of a shock at a gas stagnation pressure of 0.85 bar.

Table 8.3: Flow characteristics within the shock layer.

Condition	p_{sh} [mbar]	T_{sh} [K]	ρ_{sh} [kg m ⁻³]	$n_{Ar,sh}$ [m ⁻³]	u_{sh} [m s ⁻¹]
1	11.6	518	$1.07 \cdot 10^{-2}$	$1.60 \cdot 10^{23}$	1511
2	9.63	665	$6.95 \cdot 10^{-3}$	$1.04 \cdot 10^{23}$	1712
3	7.36	772	$3.59 \cdot 10^{-3}$	$6.86 \cdot 10^{22}$	1844



Fig. 8.10: View of the experimental set up.

8.5 CCD Imaging

In order to study the MHD interaction, imaging of the shock is accomplished by means of a fast shutter CCD camera. A PCO SensiCam SVGA interline CCD color camera, capable of a minimum exposure time of 100 ns is utilized. The quantum efficiency peak is nearly 43% at a wavelength of 380 nm. All images are taken by means of a Pentax 35-80 mm – f 3.5 zoom lens.

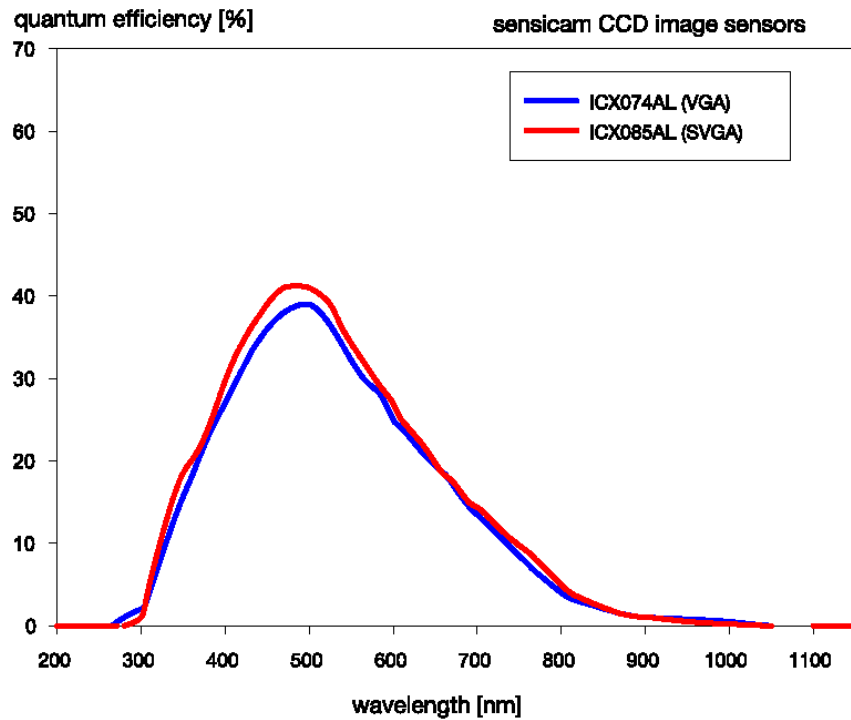


Fig. 8.11: CCD quantum efficiency.

The camera can also be coupled with a filter characterized by a wavelength threshold of 650 nm. Radiation with wavelengths larger than the threshold passes through the filter, radiation with lower wavelengths does not go through it. Most ion lines have wavelength below the threshold and the filter stops them. Actually most images are performed without using the filter.

8.6 Emission Spectroscopy Set-Up

In order to gain information of the plasma properties, emission spectroscopy was used. Two different instruments were utilized, leading to complimentary sets of data.

Time resolved emission spectroscopy was performed by means of a monochromator coupled with a photomultiplier. The monochromator was a Jobin Yvon HR460, a 460mm focal length instrument with a focal ratio of F5.3, based on a Czerny Turner configuration. Two gratings were used, both holographic: a 1200 lines/mm (that leads to a linear dispersion of 1.74nm/mm) and a 2400 lines/mm. Bandwidth of the instrument was settled to 0.523nm for all the lines except for Argon II, at is 0.342nm. The photomultiplier was a

Hamamatsu R984P, sensible within the wavelength range of 194nm to 800nm, with peak sensitivity around 400nm.

With this monochromator, it is possible to record the time behaviour of just one line of emitted spectra, once it was centred on its wavelength: therefore its limit consist on the impossibility to record the overall spectra at the same time. For this an optical multichannel analyzer (OMA) based on a Czerny Turner symmetrical configuration was used.

An entrance slit 25 μ m broad, in conjunction with a 600lines/mm grating allowed to recording the simultaneous of the spectra confined between 350nm and 1000nm with a FWHM resolution of 1.5nm. This OMA is coupled with a linear CCD array of 2048 pixels, with a minimum exposure time of 2ms. It is clear that with this instrument any time-resolved analysis is precluded, as well as a precise scansion in wavelength for a precise discerning in emitted peaks. An OMA shutter was fully synchronized with the current devoted to the creation of the magnetic field.

Light was collected from the shock region at the same position of the first hall electrode by means of a small lens (25mm focal length F4) coupled with a optical fibre This lens focuses rays perpendicular to the flow direction. The optical fibre exits the vacuum vessel by means of a vacuum feed through, directly to the spectra recording instrument. It is possible to see the position of the light spot detected in figure 8.12.

Both instruments were calibrated in absolute intensity by means of a deuterium/halogen lamp as well as in wavelength by means of an argon/mercury lamp.

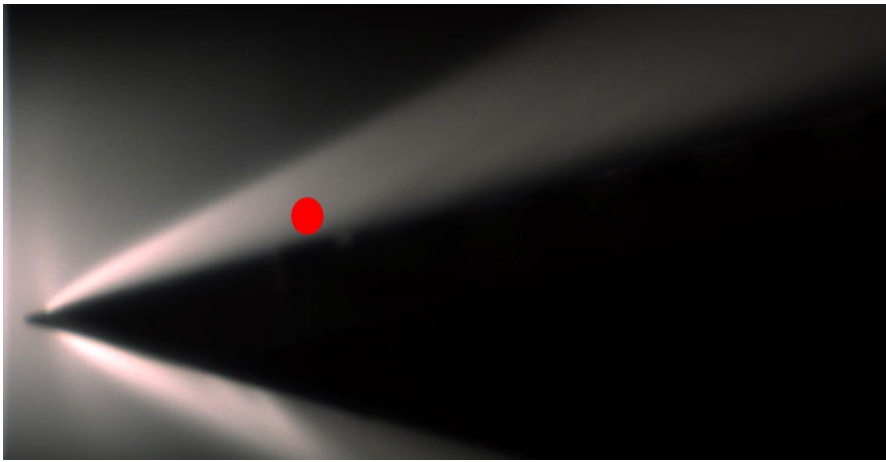


Fig 8.12: Plasma volume under investigation in spectra analysis.

9. Results: Imaging and Electrical Measurements

9.1 Shock Front Imaging

In order to investigate the influence of the MHD interaction on the shock created by the test body in the argon flow at Mach 6, images of the shock with and without the magnetic field are compared. In figure 9.1 two images are superimposed. Both shocks are obtained in condition 3 ($p_{tot} = 0.65$ bar). For the shock with magnetic field, B is equal to 0.35 T. The MHD interaction causes an increase of the shock front angle.

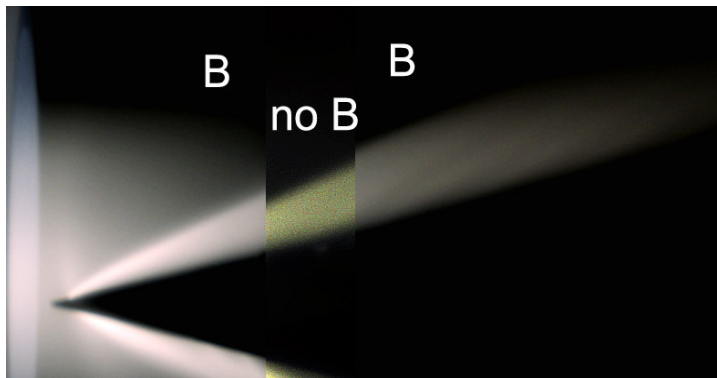


Fig. 9.1: Superimposed images of the shock with and without magnetic field: the experimental condition 3 ($p_{tot} = 0.65$ bar) produces both for the case with magnetic field is $B = 0.35$ T.

In figure 9.2 and 9.3 the comparison regards condition 2 ($p_{tot} = 0.85$ bar). In this case the increase of the shock front angle on the test body surface caused by the MHD interaction is less evident. However, when the magnetic field is on, at the leading edge of the ramp the shock appears to be much broader and the shock surface less defined.

An influence on the tip of the wedge is also clear: where the plasma is hotter and more likely to be conductive, there is the growth of some sort of a plasma wall as it is visible in figure 9.3.

In any case, however, the presence of the magnetic field corresponds also to a more pronounced optical emission. This phenomenon could be interpreted conjointly with data obtained with the optical spectrometer.

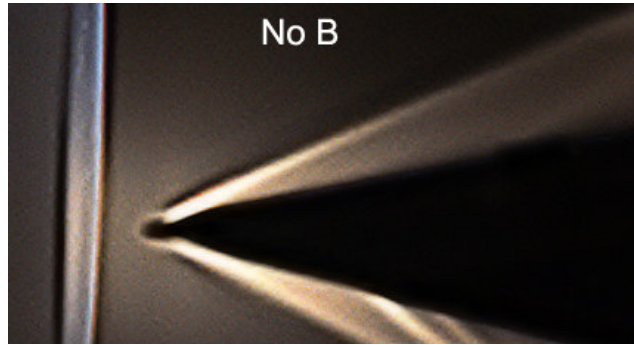


Fig. 9.2: Image of the shock without magnetic field at experimental condition 2 ($p_{tot} = 0.85$ bar).

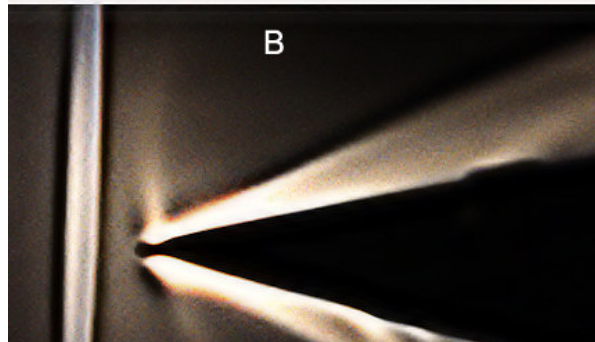


Fig. 9.3: Image of the shock with $B = 0.25$ T at experimental condition 2 ($p_{tot} = 0.85$ bar).

9.2 Electrical Measurements

Hall voltages are measured between the 1st and the 8th electrode. The measured values are very low for all experimental conditions. The Hall voltage decreases when the magnetic field increases. By means of the electric probes the electric field on the ramp surface can be determined. Figure 9.5 refers to the floating potential map for condition 2 ($p_{tot} = 0.85$ bar) and a magnetic field of 0.25 T. For the chosen electrode configuration a zero Faraday electric field (component of the electric field in the z-direction) would be expected. At all investigated conditions the Faraday field is non zero.

In order to measure the plasma resistance, the experimental setup shown in figure 9.6 is used. Measurements are taken at conditions 1, 2 and 3 for $B = 0$. For all measurements V and R are taken to be 40 V and 1000 Ω respectively. In figure 9.7 the results of the measurements are shown for the conditions 2 and 3.

For the test with $p_{tot} = 0.85$ the plasma resistance measured is 0.8 k Ω . Assuming a cross section of the plasma current of $5 \cdot 10^{-4}$ m² and a distance of

0.10 m from the upstream to the downstream electrode, a plasma conductivity of 0.20 S/m is derived.

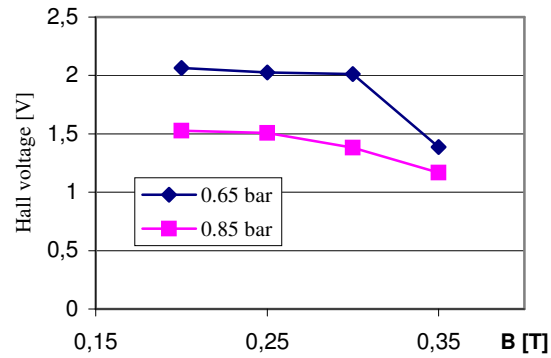


Fig. 9.4: Hall voltages measured between the 1st and the 4th electrode.

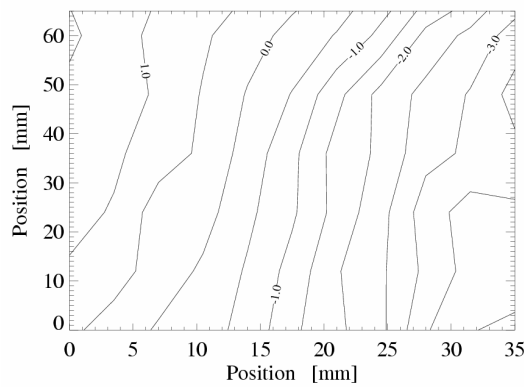


Fig. 9.5: Floating potential distribution on the test body surface for test condition 2 and $B = 0.25$ T.

By means of the five-pin probe sets placed on the test body surface the electron density of the plasma is determined. In order to do this, the five-pin balanced triple probe method is used. From the probes signals in the upstream region of the ramp, the electron density measured for $p_{\text{tot}} = 0.6$ bar is in the range between $1.5 \cdot 10^{17} \text{ m}^{-3}$ and $2 \cdot 10^{17} \text{ m}^{-3}$. In the same region for $p_{\text{tot}} = 1$ bar an electron density of about $0.5 \cdot 10^{17} \text{ m}^{-3}$ is measured.

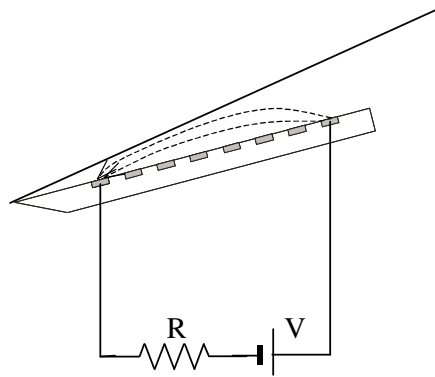


Fig. 9.6: Scheme of the experimental setup used to measure the electrical resistance of the plasma.

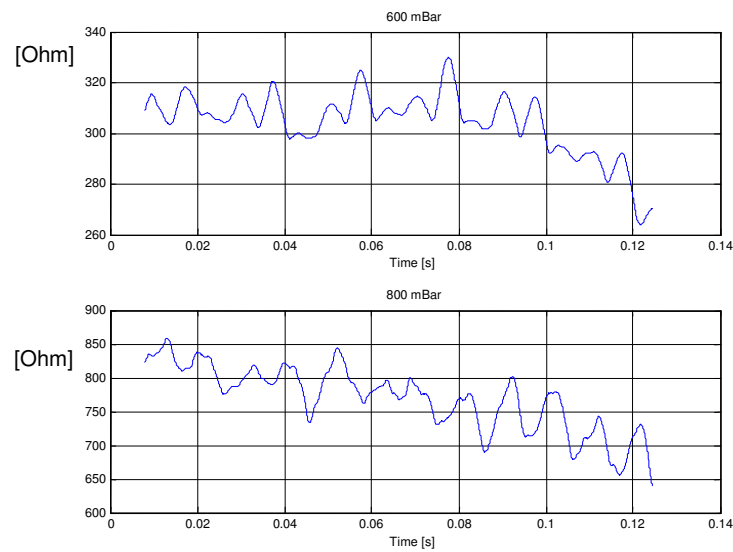


Fig. 9.7: Values of the plasma resistance measured for conditions 3 and 2.

These values decrease by a factor of 3 or 4 when the measurements are done in the downstream region. The results of the measurements agree with the results of the calculations described in the paragraph III.A.

9.3 Discussion

For the electric configuration considered, the Faraday voltage and the Hall current are kept equal to zero. Hence E_z and J_x should be zero. As a consequence the maximum value of the Faraday current density, corresponding

to $J_z = \sigma u B$, should be obtained. This maximizes the Lorentz force in the flow direction, and opposite to it, pushing the plasma away from the test body.

A very low Hall voltage and a non zero Faraday field are measured. An electrical conductivity of the order of 0.20 S/m has been derived from the measurements of figure 9.7. The conductivity obtained from the three probe method measurements is of the order of 10 S/m. This indicates that the boundary layer resistance through the test body and the core flow determines the plasma resistance measured by means of the setup of figure 9.6. Hence the plasma in the Faraday direction is not short circuited by the electrodes as shown in figure 9.6. This results in a decrease of the Faraday current. Hence a reduction of the effect of the MHD interaction is caused.

10. Plasma Emission Measurements

10.1 Signal to noise ratio

Spectra coming from OMA were an average of three measurements recorded at the same nominal conditions, plenum pressure and external magnetic field. Line intensity data from monochromator are an average over seven different shots. This was due to the necessity to improve the background noise. We consider in fact two spectra characterized by an emission line having equal signal peak S_a and equal noise N_a . The resulting signal/noise ratio S/N , average of the two measurements, is given by the following relation:

$$S/N = \frac{2S_a}{\sqrt{2N_a^2}} = \sqrt{2} \frac{S_a}{N_a} \quad (10.1)$$

So, the signal/noise ratio is raised at 1.414. Taking the average of three measurements, the S/N will be about 1.732.

10.2 Plasma Spectra

It was necessary to gain information about the behaviour of the overall plasma spectra. For doing this, the OMA device was initially used.

Exposure time was settled to its specification minimum, 2ms. With this value, it was still possible to see the influence of the magnetic field on the plasma, even if its properties are integrated: the magnetic field has a rise transient of 5 ms.

For obtaining a better signal to noise ratio, at each pressure and magnetic field condition, the final analyzed spectra were coming from the average of three different spectra, recorded with the same trigger event.

Nine different experiment conditions were chosen. When as the current in the arc heater was settled to the maximum obtainable from the power supply, the change of parameters was confined to the plenum pressure and applied magnetic field.

Three were the investigated pressures: 600mbar, 800mbar and 1000mbar. Contextually, three were the magnetic field regime chosen: 0T, 0.15T, 0.25T, where the B value is taken in the middle of the air gap between the two polar expansions.

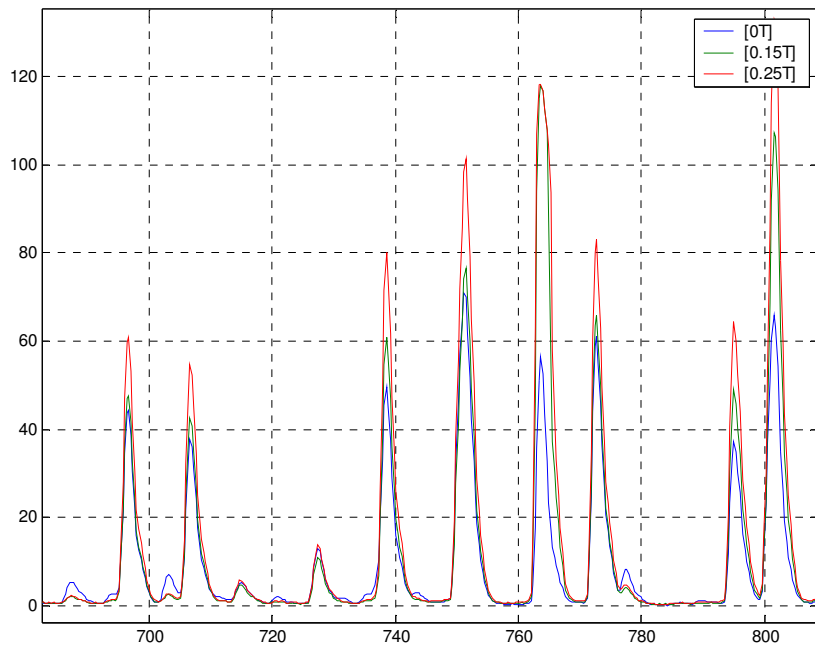


Fig. 10.1: 1000mbar plenum pressure. Argon I lines.

Higher plenum pressures thermodynamically lead to a lower temperature in the discharge chamber, due to a higher mass flow. However, a higher pressure leads to a higher mass density: this helps to obtain condition in the plasma closer to equilibrium. In this condition also, fluid dynamic properties of the flow are much more constant and reliable. But at the same time an higher temperatures leads to a higher ionization degree: therefore there must be a trade-off between those two different requirements –ionization degree and constant fluid dynamic properties–.

In the spectra there are strong contributions from neutral Argon I lines in all conditions. It is still possible to recognize several peaks of Ar II in the lower wavelength of the spectra, indicating a ionization condition of the plasma: this leads to the consideration that the plasma can not be purely radiative, a condition based on the assumption that electron number density $n_e=0$.

Even if the low resolution of the spectrograph does not allow a fine identification of all peaks, the contribution of Hydrogen *alpha* and *beta* lines is evident: hydrogen is present in the vacuum vessel mainly because of the pumping system, based on diffusive oil system.

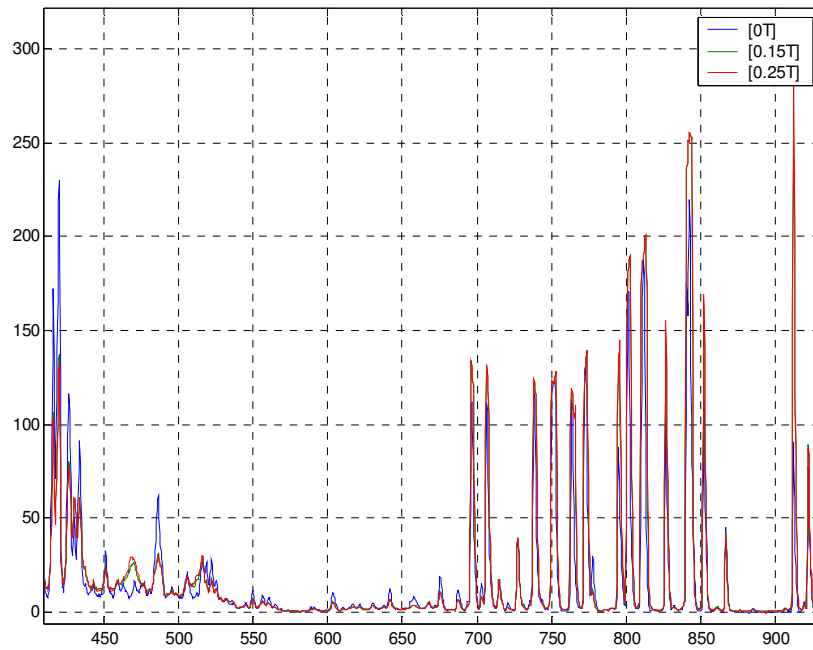


Fig. 10.2: 600mbar plenum pressure. Whole Argon spectra.

It is shown in figure 10.3 that in the lower part of the spectrum there is a contribution because of continuum emission: this radiation is coming from free to bound recombination processes.

When the magnetic field B is switched on, properties of emission spectra changes dramatically. The integral of the overall emission changes, and highness of different peaks is changing as well. Plasma behaves like there is redistribution between different energy transitions associated with different energy levels.

Time resolved emission spectroscopy seems to validate this qualitative consideration gained with OMA. Three lines were chosen, with respect to the associated transition levels: the first at low energy level, the second in the middle and the third in the upper part of the energy scheme.

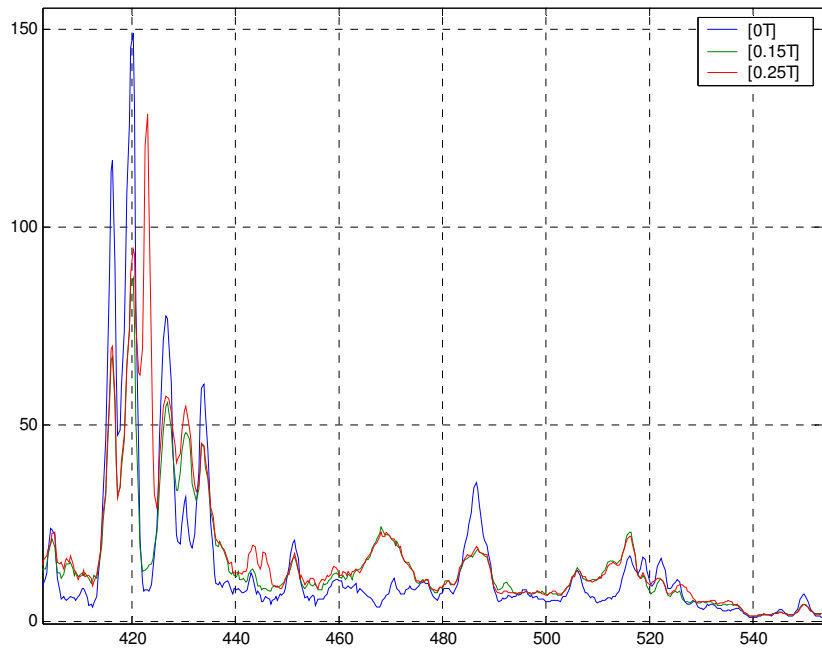


Fig. 10.3: 800mbar plenum pressure. Ions and neutral Argon lines, plus continuum emission.

At the optimum pressure for realizing the compromise between a high ionization degree (high electron temperature) and reasonably constant fluid dynamic properties (plenum pressure of 800mbar), it was chosen to also record some other lines. In particular, the time-behaviour of two Argon II lines were detected, as well as the first two lines of the hydrogen energetic scheme (H alpha and H beta in the Balmer series).

Argon ions and hydrogen lines seems to have a completely different behaviour to the more abundant Ar I lines, in the presence of the magnetic field. Argon ions seems not to be affected by the its presence, while hydrogen lines show a superimposition of the variations due to B field dependency and a changing due to time dependency. It is clear that those emissions are affected by some kind of transient phenomenon.

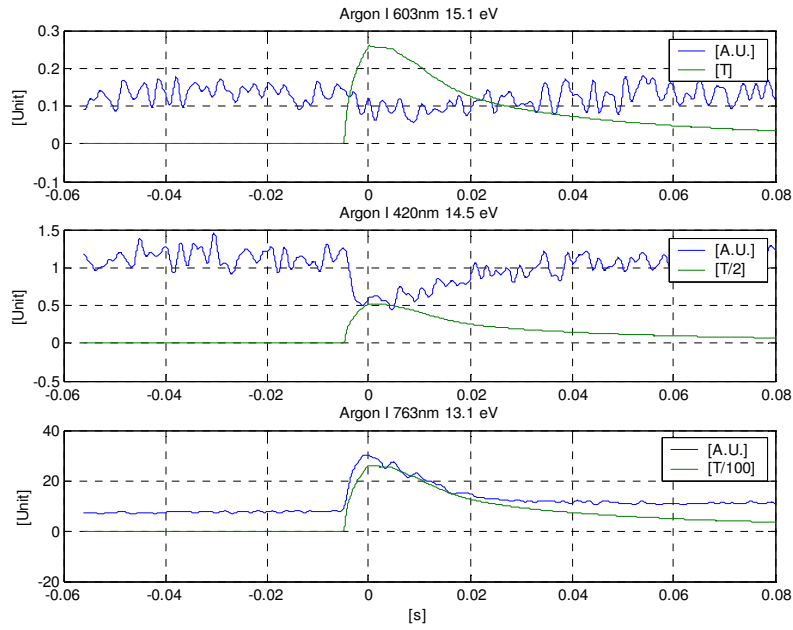


Fig. 10.4: 600mbar plenum pressure, 0.15 T. Argon I time-resolved line emission.

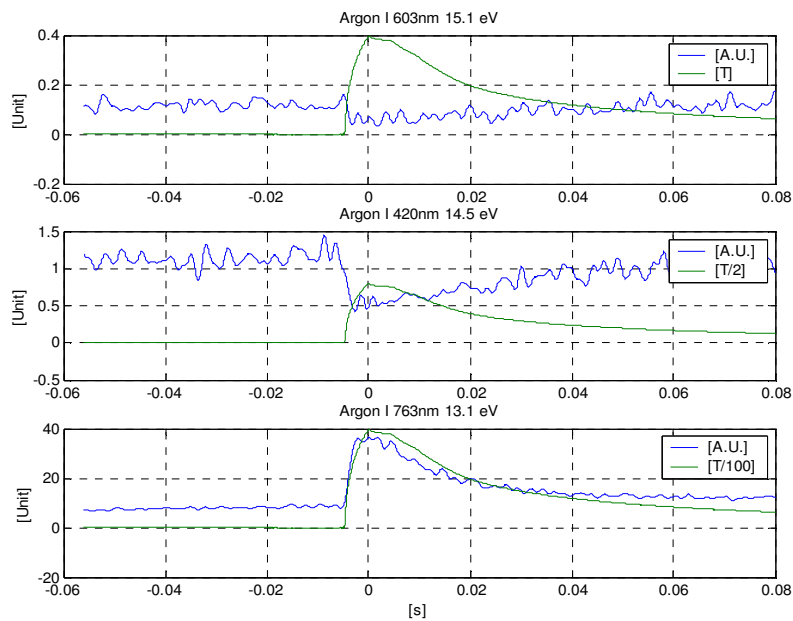


Fig. 10.5: 600mbar plenum pressure 0.25 T. Argon I time-resolved line emission.

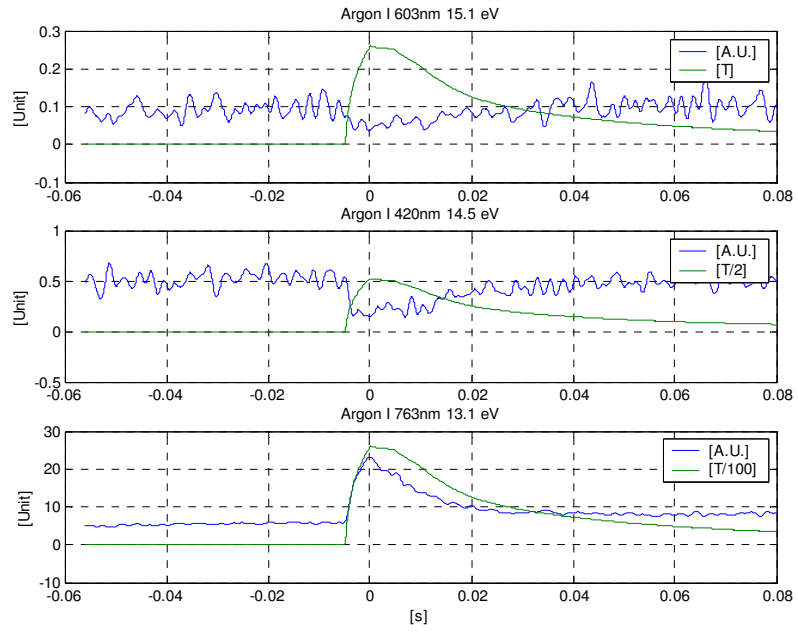


Fig. 10.6: 800mbar plenum pressure, 0.15 T. Argon I time-resolved line emission.

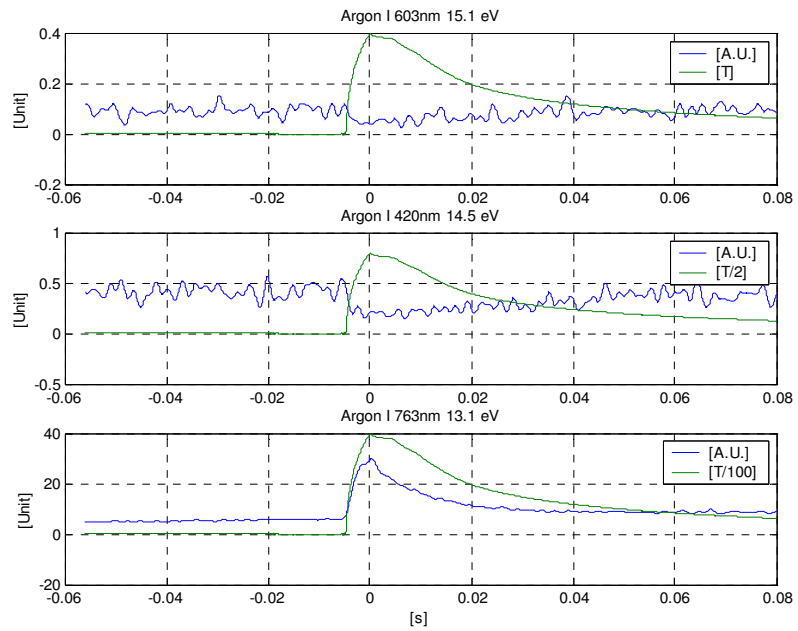


Fig. 10.7: 800mbar plenum pressure, 0.25 T. Argon I time-resolved line emission.

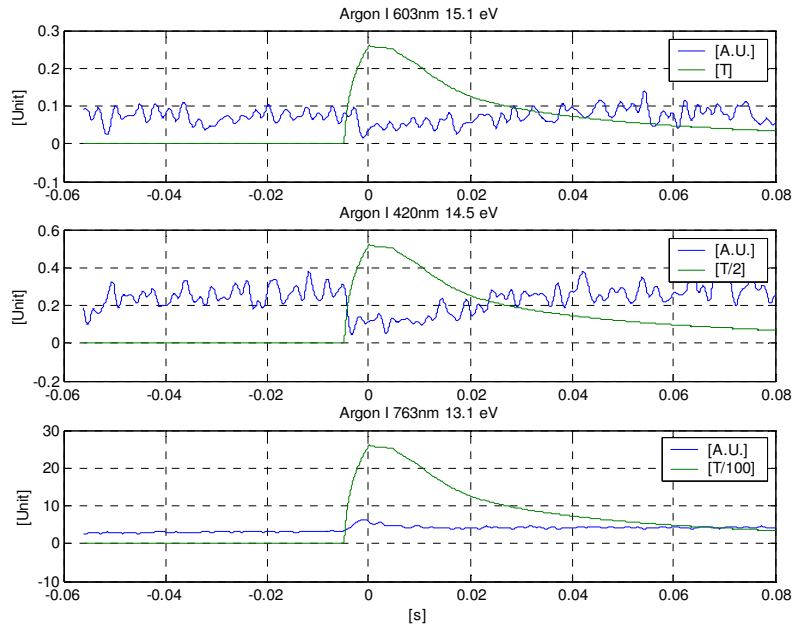


Fig. 10.8: 1000mbar plenum pressure, 0.15 T. Argon I time-resolved line emission.

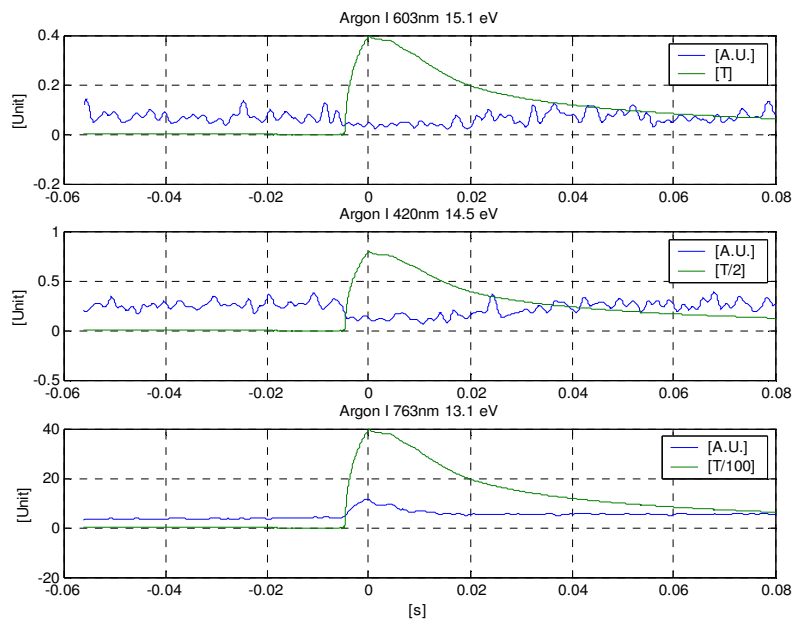


Fig. 10.9: 1000mbar plenum pressure, 0.25 T. Argon I time-resolved line emission.

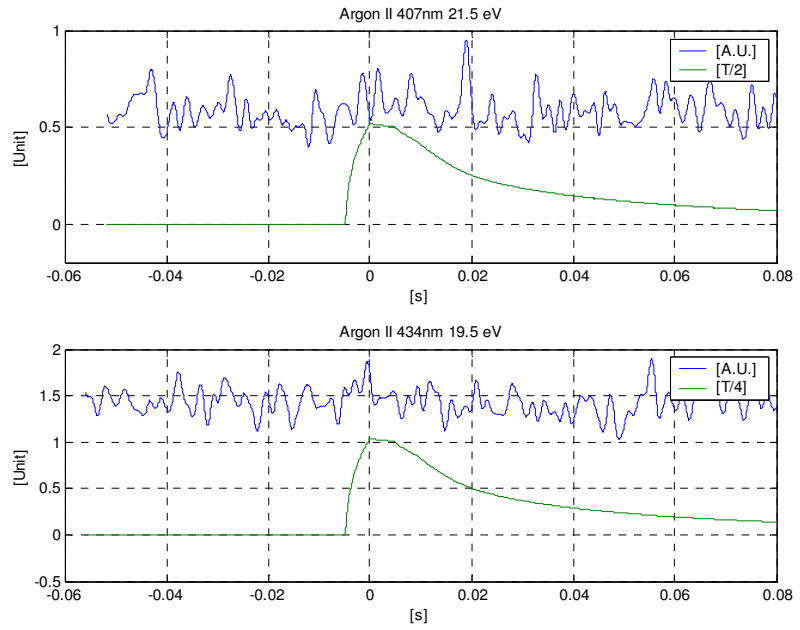


Fig. 10.10: 800mbar plenum pressure, 0.15 T. Argon II time-resolved line emission.

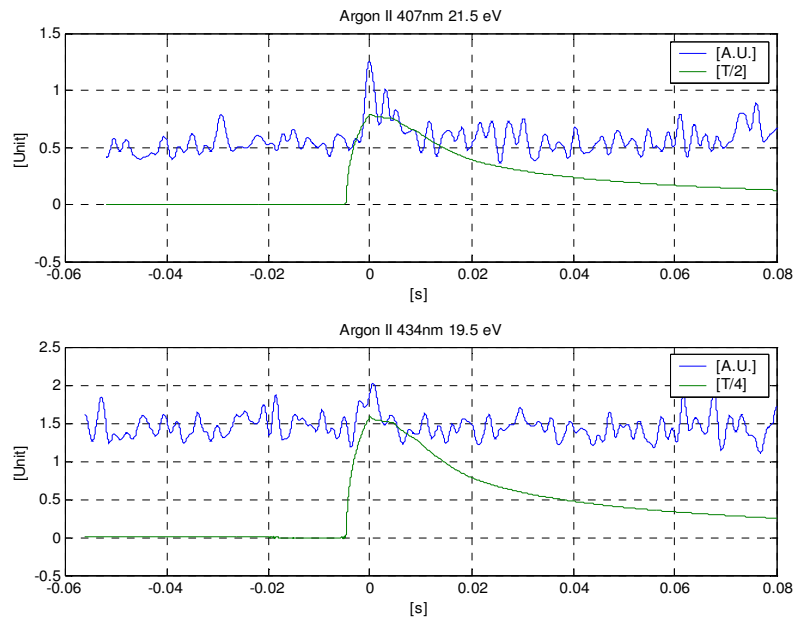


Fig. 10.11: 800mbar plenum pressure, 0.25 T. Argon II time-resolved line emission.

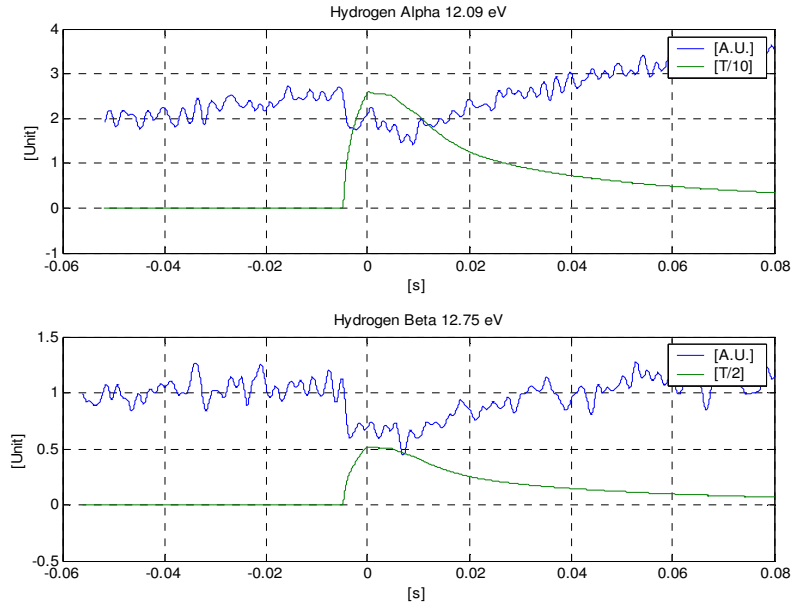


Fig. 10.12: 800mbar plenum pressure, 0.15 T. Hydrogen I time-resolved line emission.

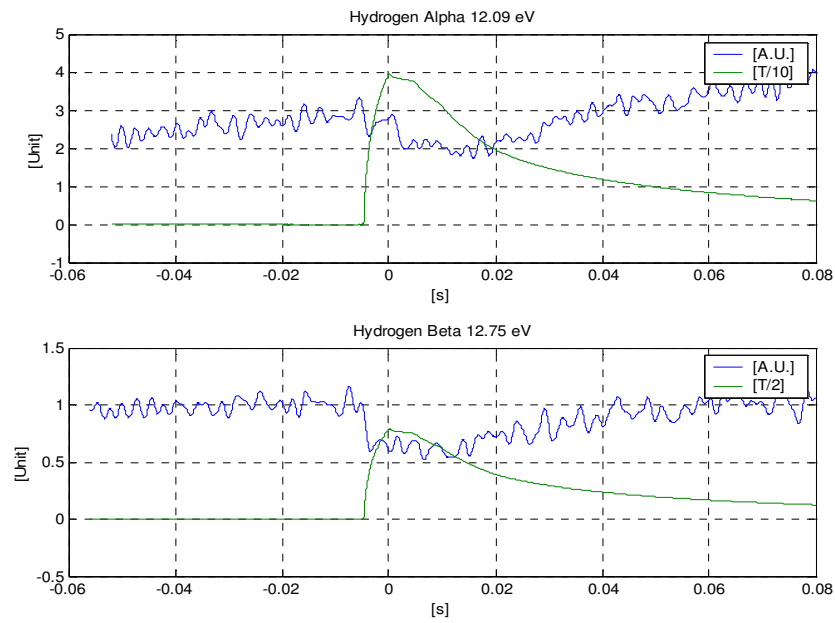


Fig. 10.13: 800mbar plenum pressure, 0.25 T. Hydrogen I time-resolved line emission.

10.3 Calculation of the plasma parameters

A plasma parameter of great interest is the electron temperature that is determined by means of the Boltzmann plot. The radiation intensity of a generic emission line I_n is in fact is proportional to the spontaneous emission probability $A^{n \rightarrow l}$ and to the population density of the up level of the transition n_n :

$$I_n = c_1 A^{n \rightarrow l} n_n \frac{hc}{\lambda_n} \quad (10.2)$$

If the particle densities are distributed over the energy levels as Boltzmann distribution, then the following relation holds:

$$\frac{n_n}{n_0} = \frac{g_n}{g_0} e^{-\frac{E_n - E_0}{kT_e}} \quad (10.3)$$

where T_e is the electron temperature. After the substitution of equation 10.3 into 10.2, the following relation is obtained:

$$y_n = \ln \left(\frac{I_n \lambda_n}{A^{n \rightarrow l} g_n} \right) = C - \frac{E_n}{kT_e} \quad (10.4)$$

Each equation (10.4) represents a point (E_n, y_n) in a semi-logarithm plot (also called Boltzmann plot). The slope of the line fitting the data, obtained by several emission lines, is proportional to the electron temperature. If the points are perfectly aligned, the plasma is in partially local thermodynamic equilibrium (pLTE). Deviations from this equilibrium condition are reflected in the Boltzmann plot by a scattering of the points. In this case, the plasma is not characterized by a unique temperature and it is more appropriate to speak of excitation or population temperature.

An estimation of the electron density could be carried out by means of the ratio of two emission lines of the same element, but proper to different systems (for example neutral and singly ionized). If the plasma is in local thermodynamic equilibrium (LTE), the neutral and singly ionized particle density, n_0 and n_+ respectively, are related together the by the Saha equation:

$$\frac{n_e n_+}{n_0} = \frac{2U_+}{U_0} \left(\frac{m_e k T_e}{2\pi h^2} \right)^{3/2} \exp\left(-\frac{\chi_i - \Delta\chi_i}{k T_e} \right) \quad (10.5)$$

where χ_i is the ionization potential and $\Delta\chi_i$ is the reduction in χ_i due to Coulombian interactions. Writing relation 10.5 for a neutral and singly ionized line and combining the ratio with 10.3, the following relation is obtained:

$$n_e = \frac{A_{+k} g_{+k} \lambda_n}{A_n g_n \lambda_{+k}} \frac{2I_n}{I_{+k}} \left(\frac{m_e k T_e}{2\pi h^2} \right)^{3/2} \exp\left(-\frac{E_{+k} - E_n + \chi_i - \Delta\chi_i}{k T_e} \right) \quad (10.6)$$

Finally, the neutral density n_0 , and then the ionization degree of the plasma, can be evaluated by means of the Saha equation. The validity of this method depends on the validity of the condition of pLTE for the levels of the transitions considered. It is well known from the theory of collisional-radiative processes that the upper levels of an atom reach a thermal distribution with the continuum of free electrons more easily than the lower levels. Thus, it is possible to define the levels of an atom as being in pLTE from level p if equation 10.6 applies to it and all higher-lying levels. Many authors studied this problem. Griem, for example, studied how the emission of radiation affects the distribution with respect to excited states in hydrogen (or hydrogen-like ions) plasma. He found the following relation:

$$N_e \geq 7 \times 10^{18} \frac{z^7}{p^{\frac{17}{2}}} \left(\frac{k T_e}{z^2 E_H} \right)^{\frac{1}{2}} \text{ cm}^{-3} \quad (10.7)$$

where E_H is the hydrogen ionization energy and p is the effective principal quantum number defined as:

$$p = Z \sqrt{\frac{E_H}{E_{ion} - E_p}} \quad (10.8)$$

Other criteria are presented by Wilson, Drawin, Biberman, McWirtter and recently by Fujimoto. For atoms or ions that are not hydrogen-like, such as the ArII system, the applicability of these criteria is a critical point. Experiments on ArII, in fact, show that the criterion 10.7 is too restrictive.

Another way to calculate the electron density is based on the line broadening theories. This method is preferable because it does not require any hypothesis on the equilibrium condition in the plasma. Unfortunately, the OMA spectral resolution is in the range of 1.5-2.5 nm, too high to measure the line broadening.

10.4 Continuum Emission

Apart from line emission, the plasma also emits continuum radiation. This consists of recombination emission and Brehmsstrahlung. The recombination-emission is generated when a free electron and an ion recombine to a neutral atom or an ion with charge $Z-1$. In the plasmas under study, only singly ionised species will be present so that $Z=1$. The emission coefficient $\varepsilon_{fb,\lambda}$ of this recombination emission is equal to

$$\varepsilon_{fb,\lambda}(\lambda, T_e) = \frac{c_1 n_e n_i}{\lambda^2 \sqrt{T_e}} \left[1 - \exp\left(-\frac{hc}{\lambda k T_e}\right) \right] \xi_{fb}(\lambda, T_e) \quad (10.9)$$

where $\xi_{fb}(\lambda, T_e)$ is the free bound Bibermann factor which is a dimensionless quantity close to unity. For an argon plasma $\xi_{fb}(\lambda, T_e) = 1$ and emission is in the range $\lambda > 300 \text{ nm}$. The subscript fb is an abbreviation for free-bound, which refers to the state of the electron before (free) and after (bound) the emission. In this equation n_i is the total density of ions. This number can be replaced by the electron density under the assumption that all ions are singly ionised and that the plasma is quasi neutral. This assumption is also made for the rest of this study. The constant c_1 is equal to:

$$c_1 = \frac{16\pi e^2}{3c^2 m_e (6\pi m_e k)^{1/2} (4\pi \varepsilon_0)^3} = 1.6321 \cdot 10^{-43} \text{ Jm}^4 \text{ K}^{1/2} \text{ s}^{-1} \text{ sr}^{-1} \quad (10.10)$$

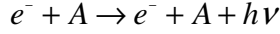
Brehmsstrahlung originates from a change of the momentum of electrons caused by an interaction of electrons (e) with neutral atoms (a) or ions (i). We first consider the e-i interaction. The process of Brehmsstrahlung by the interaction of electrons with ions is represented by



During this Coulomb interaction, the energy of the electron reduces and is transferred to the photon. The emission coefficient for the Coulomb interaction is represented by

$$\mathcal{E}_{ff,\lambda}^{ei}(\lambda, T_e) = \frac{c_1 n_e^2}{\lambda^2 \sqrt{T_e}} \exp\left(-\frac{hc}{\lambda k T_e}\right) \xi_{ff}(\lambda, T_e) \quad (10.12)$$

In his equation, $\xi_{ff}(\lambda, T_e)$ is the free-free Bibermann factor, and the value of c_1 is equal to that of the fb Bibermann factor. Because the electron is not bound by this interaction the subscript ff (free-free) is added to the emission coefficient. The other component of the bremsstrahlung is generated by the interaction of electrons and atoms and is represented by



The emission coefficient of the electron-atom (ea) interaction is given by

$$\mathcal{E}_{ff,\lambda}^{ea}(\lambda, T_e) = \frac{c_2 n_e T_e^{3/2} n_a Q(T_e)}{\lambda^2} \left[1 + \left(1 + \frac{hc}{\lambda k T_e} \right)^2 \right] \exp\left(-\frac{hc}{\lambda k T_e}\right) \quad (10.13)$$

The parameter Q in equation 10.13 represents the cross section of momentum transfer from electrons to neutral atoms. For argon, it can be approximated by

$$Q(\hat{T}_e) = \sqrt{\frac{8}{3\pi} \left(\frac{5}{(1+19.73\hat{T}_e)^2} \right)} - 0.3 + 3.25\hat{T}_e - 0.064\hat{T}_e^3 \cdot 10^{-20} m^{-2} \quad (10.14)$$

where the electron temperature \hat{T}_e is given in eV. Equation (4.14) only holds under the assumption that an integration of Q over the electron velocity can be replaced by taking the value of Q at the average electron velocity. The coefficient c_2 is given by

$$c_2 = \frac{32e^2}{12\pi\epsilon_0 c^2} \left(\frac{k}{2\pi m_e} \right)^{3/2} = 1.026 \cdot 10^{-34} \text{ Jm}^2 \text{ K}^{-3/2} \text{ s}^{-1} \text{ sr}^{-1} \quad (10.15)$$

The measured continuum emission coefficient is determined by the sum of the various components, i.e.

$$\mathcal{E}_{total,\lambda} = \mathcal{E}_{fb,\lambda} + \mathcal{E}_{ff,\lambda}^{ei} + \mathcal{E}_{ff,\lambda}^{ea} \quad (10.16)$$

If the electron temperature which is calculated by other measurements is inserted into equations (10.9), (10.12), (10.13) and (10.14), the only unknown is the electron density. Thus continuum emission provides a means to determine the electron density.

10.5 Plasma parameters

As mentioned before, the selections of the Argon I lines were made taking into account the energy level as well as the possibility of isolating them by means of the monochromator resolution. In table 10.1 the detailed properties of the transition considered are shown, with the aim of building the most precise Boltzmann plot possible.

Tab 10.1: Argon I lines recorded by means of monochromator.

Wavelength (nm)	A_{ki} (10^8s^{-1})	$E_i - E_k$ (eV)	Configurations	Terms	$J_i - J_k$
420.0675	9.67e-03	11.54835 - 14.49905	3s2.3p5(2P* <3/2>)4s - 3s2.3p5(2P* <3/2>)5p	2[3/2]* - 2[5/2]	2 - 3
603.2127	9.67e-03	13.07572 - 15.13054	3s2.3p5(2P* <3/2>)4p - 3s2.3p5(2P* <3/2>)5d	2[5/2] - 2[7/2]*	3 - 4
763.5105	2.45e-01	11.54835 - 13.17178	3s2.3p5(2P* <3/2>)4s - 3s2.3p5(2P* <3/2>)4p	2[3/2]* - 2[3/2]	2 - 2

As it is possible to see, there are strong deviations from Boltzmann plots over lower and upper levels in the energy scheme. In particular, the lower the plenum pressure, the higher the difference between excitation temperatures computed from higher and lower levels. Due to the equation expressed in 6.25, the principal quantum number limit for a collisional to radiative process is

equal to 4. This means from the energy level diagram that just the two higher lines recorded lie beyond this limit in it. The lower line is dominated by radiative processes that further deviate its behaviour from Boltzmann equilibrium. So even if there is a total absence of a Local Thermodynamic Equilibrium, the fact that collisional processes are leading means that the excitation temperature estimated by the higher level Boltzmann plot should not be so far from true electron temperature. Moreover, due to hot to cold transition, the lines chosen relate to the second quadrant of the domain plane. This means that even if kinetics is collisionally dominated, it is not in a pLTE condition and the excitation temperature computed could not be considered to be the electron temperature.

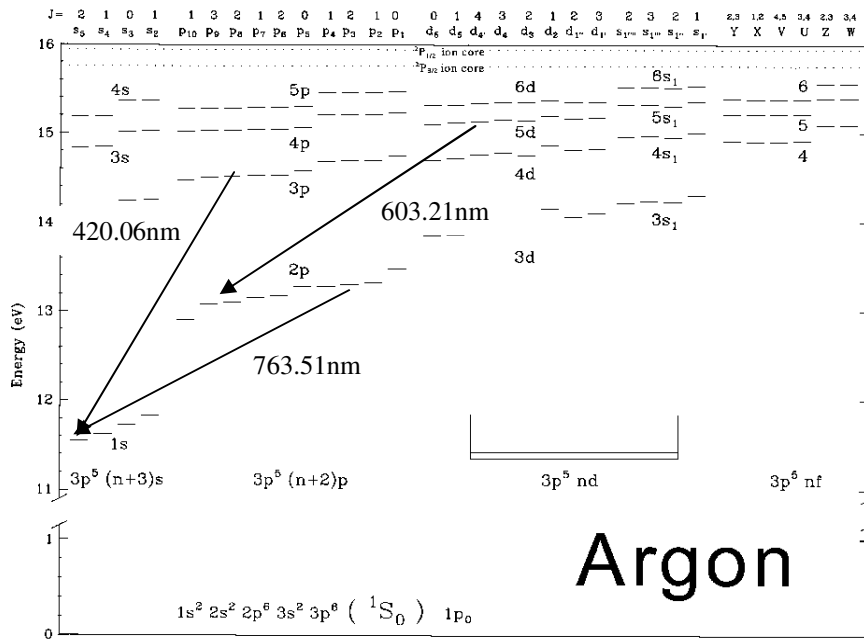


Fig 10.14: Argon I energy diagram, and the three lines recorded with monocromator.

To take into account the effect of the B field, one has to consider the dominant improper balance ruling in the plasma before its presence: plasma is dominated by means of recombination-deexcitation processes (lies in cold CRC-DSB of the domain plane). This means that the ground state of Argon II can be considered as the source of Argon I excited states. When the magnetic field is switched on, the first particles to detect its presence are electrons. Due to the very high mobility of electrons (low pressure, few Torr), it should not be wrong to state that their permanence time in an elementary volume is longer:

this leads to a higher net number of collision with heavy particles. In this non-equilibrium process, let excitations of Argon I as well as Argon II from the ground state occur: this can be seen by the low energy line emission that is rising by a factor of 4. However, Argon II ground state can be considered as a source of excitation from higher energy Ar I states. But population density of Ar II ground state decreases because of electron collision, and with it also excitation processes for high energy Argon I transitions: this is the reason for which there is a slight depauperation in those levels. It has to be said that the ionization degree is very low, and for this reason this depauperation does not propagate to a further deviation from high energy line-to-line equilibrium as is the case for lower levels. This is the reason for which, in the higher part of Boltzmann plot, the presence of the B field can not be seen as it can for lower levels.

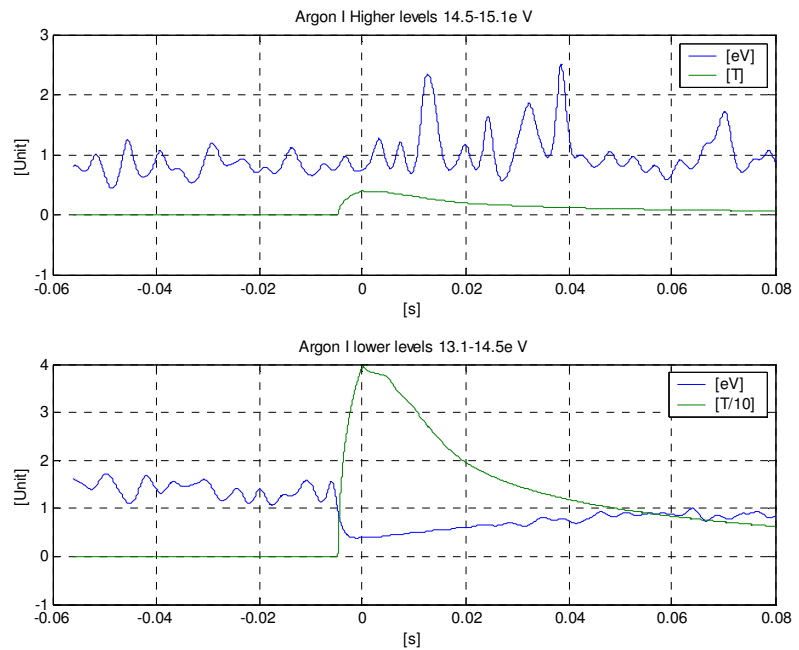


Fig 10.15 : Excitation temperature. 800 mbar plenum pressure, 0.25T.

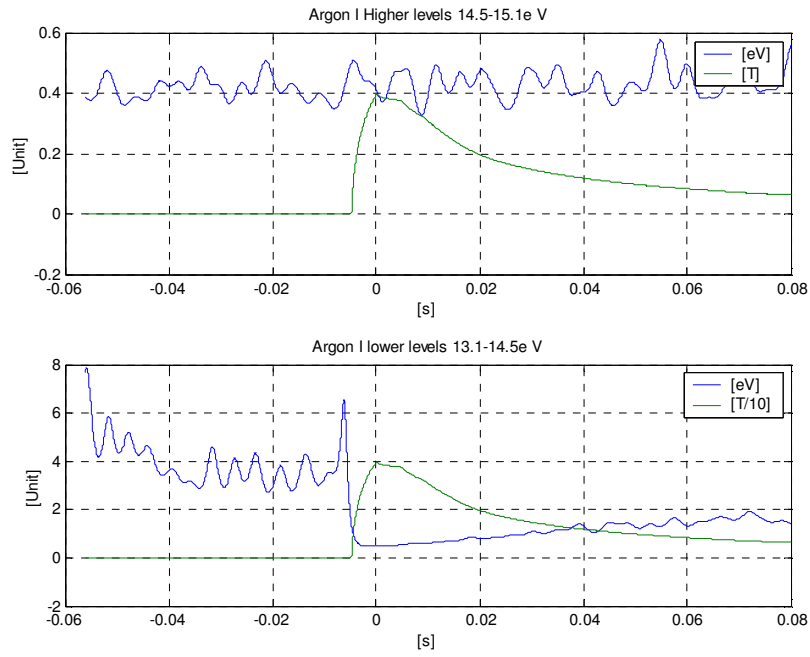


Fig 10.16 : Excitation temperature. 600 mbar plenum pressure, 0.25T.

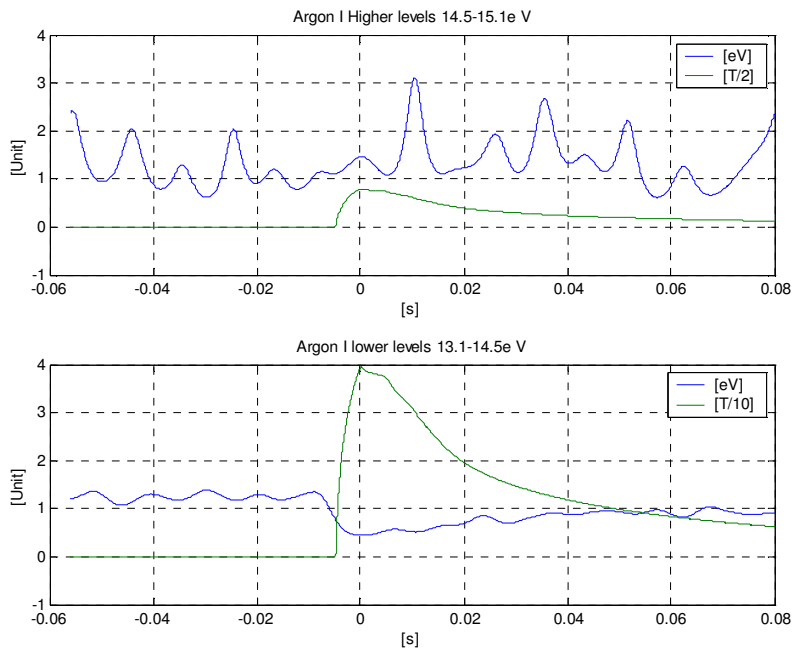


Fig. 10.17 : Excitation temperature. 1000 mbar plenum pressure, 0.25T.

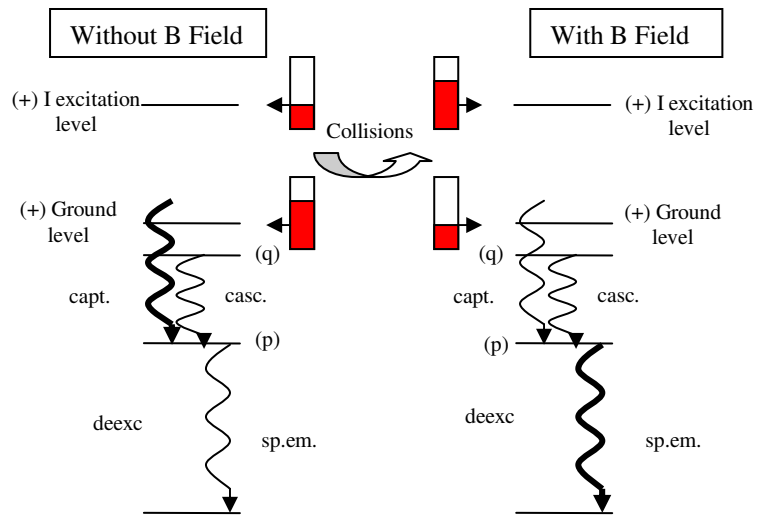


Fig. 10.18: Changes in excitation process with and without B field.

As further proof of this, in figure 10.19 shows the ratio computed as follows:

$$ratio = \left(\frac{n_{up}}{n_{low}} \right)_{measured} // \left(\frac{n_{up}}{n_{low}} \right)_{Boltzmann} . \quad (10.17)$$

This is evidence that lower levels are further from some kind of equilibrium reached from higher levels.

It is also noticeable that the ratio of higher levels is almost insensible to the non equilibrium processes that affect the plasma.

At 800mbar plenum pressure, there is data also from the Argon II and Hydrogen lines. In this case all the energy level transitions are related to principal quantum number that lies below the collisional limit, and indications of excitation temperatures simply do not hold.

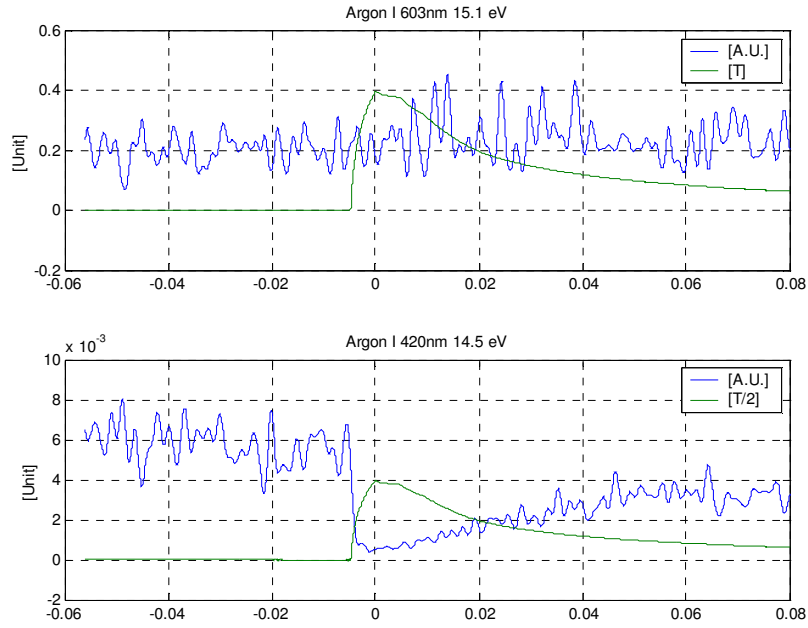


Fig. 10.19: Deviations from Boltzmann equilibrium. 800 mbar plenum pressure, 0.25T.

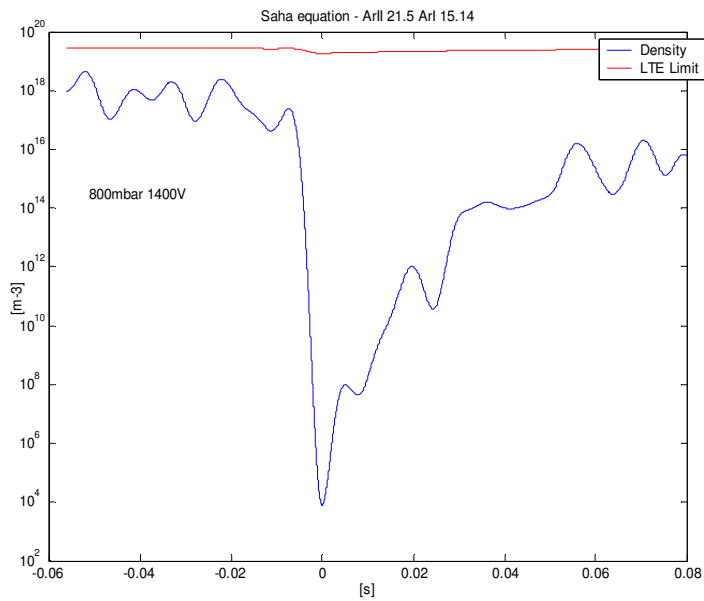


Fig. 10.20: Time-resolved electron number density by means of Saha. Plotted with Griem criteria for LTE plasmas. 800 mbar plenum pressure, 0.25T.

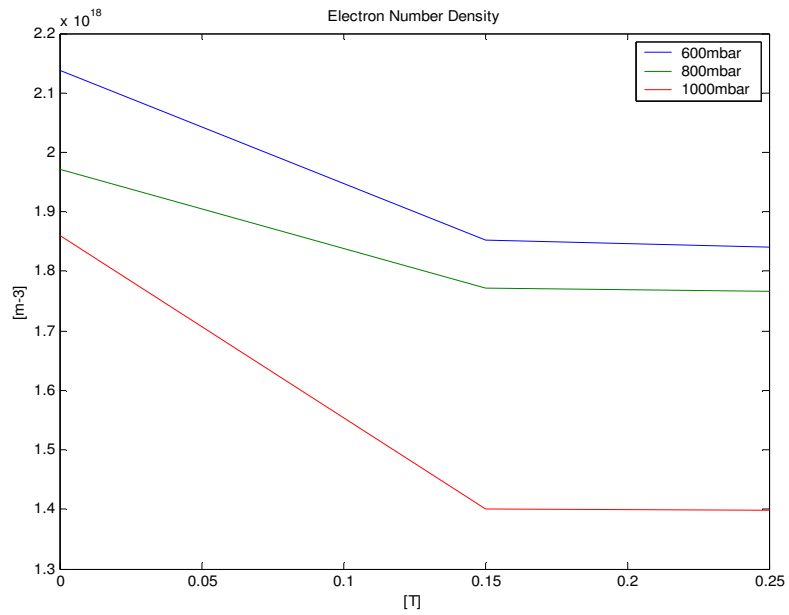


Fig. 10.21: Electron number density n_e by means of continuum (523nm) under the assumption of $n_e=n_i$.

Electron number density was computed by means of Saha law and continuum radiation. However, both calculations have to be considered as mere indications. Saha law is not valid, and as plotted in figure 10.20, density lies far under the validity limit founded with Griem criteria.

Unfortunately, even the density calculated by means of continuum radiation is tricky: the minimum requirement of this technique is the existence of a pLTE condition with a unique electron temperature, and as stated previously this conditions does not hold.

It has to be said that those two methods, whenever both intrinsically dubious, lead to the same order of magnitude in electron number density

10.6 Optical Multichannel Analyzer

The same measurements were performed by means of the optical multichannel analyzer. In this case, spectra recorded were time integrated in order to obtain a significantly high signal to noise ratio: gating time was of 2ms. Triggering was synchronized with the magnetic field by means of the oscilloscope.

Spectra coming from subsequent experimental shots at the same nominal conditions were averaged in order to smooth differences due to the turbulent-like fluid dynamic behaviour of the high enthalpy wind tunnel, in particular at low pressure.

When the magnetic field was switched on, line emission was noticeably higher, saturating the OMA signals. Only few lines can be chosen for building up a Boltzmann plot, as it shown in tables 10.2 and 10.3. Moreover, the OMA is limited by spectral resolution: lines are not well defined. Therefore, data obtained from the OMA are not reliable as data obtained by means of the monochromator.

Magnetic fields data are even more uncertain, because of some saturation problems. The displayed results are related to a 2ms gating time, in which the magnetic field varies considerably.

Tab 10.2: Argon I selected lines for Boltzmann plot with OMA.

Wavelength (nm)	E_{up} (eV)	A_{ki} ($10^8 s^{-1}$)	J_{up}
978.45	13.09576	1.60E+06	2
965.7786	12.90789	5.98E+06	1
922.4498	13.17267	5.88E+06	2
919.46	14.25605	1.98E+06	1
852.1441	13.28354	1.47E+07	1
591.2000	15.00458	1.03E+06	1

Tab 10.3: Argon II selected lines for Boltzmann plot with OMA.

Wavelength (nm)	E_{up} (eV)	A_{ki} ($10^8 s^{-1}$)	J_{up}
487.9863	19.68138	9.53E+07	2.5
458.9898	21.12846	1.05E+08	2.5
434.8064	19.49585	1.30E+08	3.5

Tab 10.4: Summary of excitation temperatures in eV among various conditions.

Ar I	[0 T]	[0.15 T]	[0.25T]
600mbar	1.186321	0.781776	0.775781
800mbar	1.250642	0.826906	0.81634
1000mbar	1.271474	0.811746	0.792007

Ar II	[0 T]	[0.15 T]	[0.25T]
600mbar	1.3216	2.105614	2.090693
800mbar	1.314654	2.34388	2.548699
1000mbar	1.867401	2.421699	2.297599

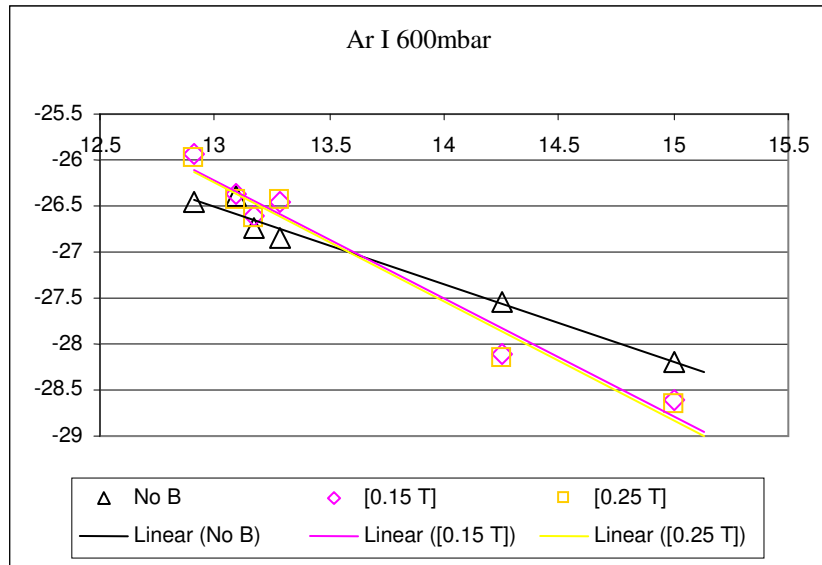


Fig. 10.22: Boltzmann plot for Ar I. Plenum pressure 600mbar.

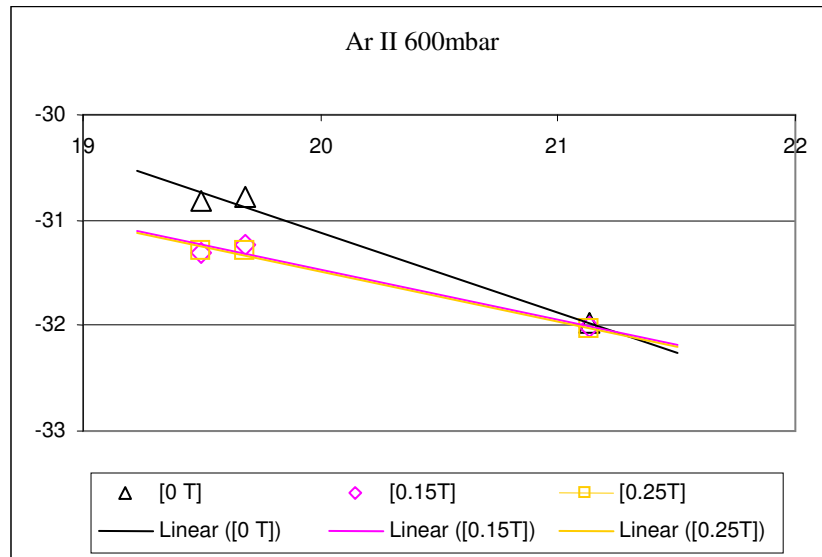


Fig. 10.23: Boltzmann plot for Ar II. Plenum pressure 600mbar.

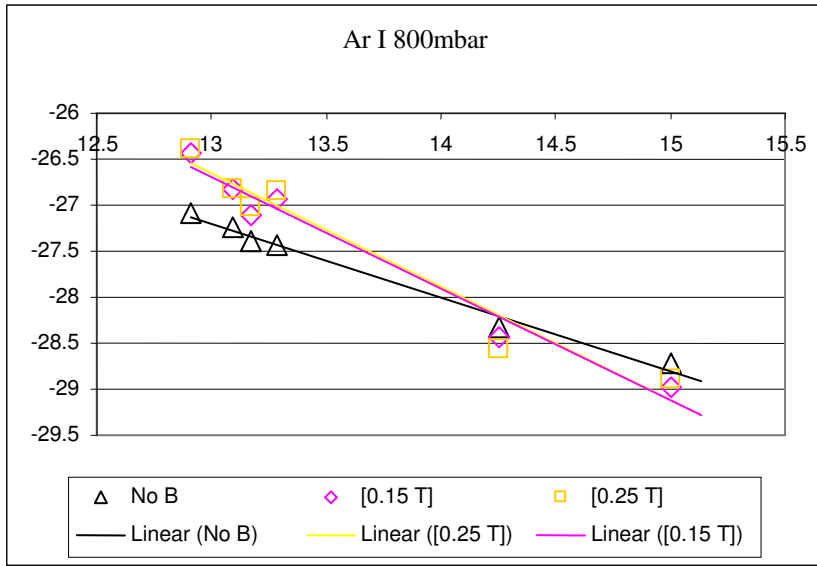


Fig. 10.24: Boltzmann plot for Ar I. Plenum pressure 800mbar.

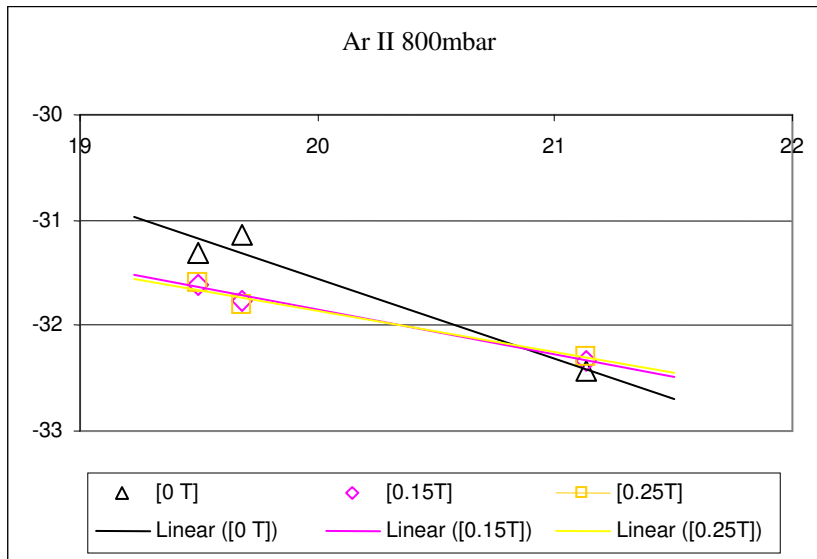


Fig. 10.25: Boltzmann plot for Ar II. Plenum pressure 800mbar.

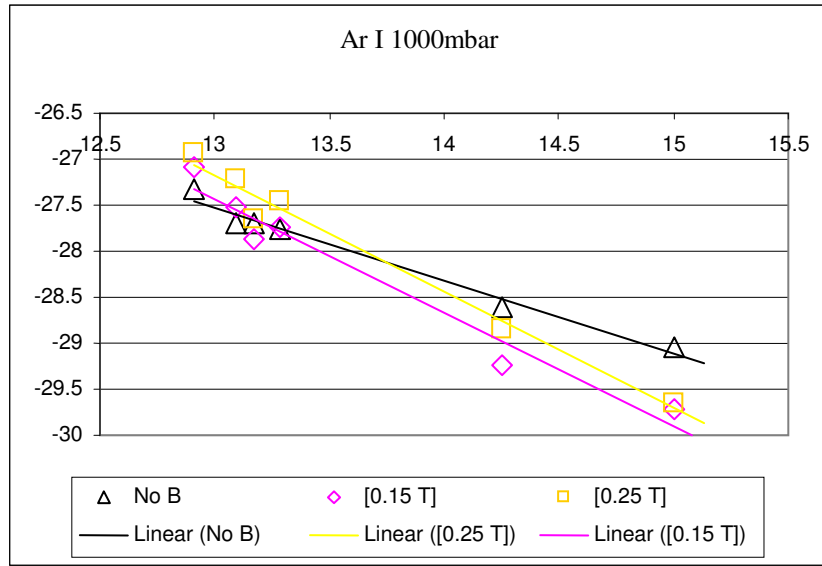


Fig. 10.26: Boltzmann plot for Ar I. Plenum pressure 1000mbar.

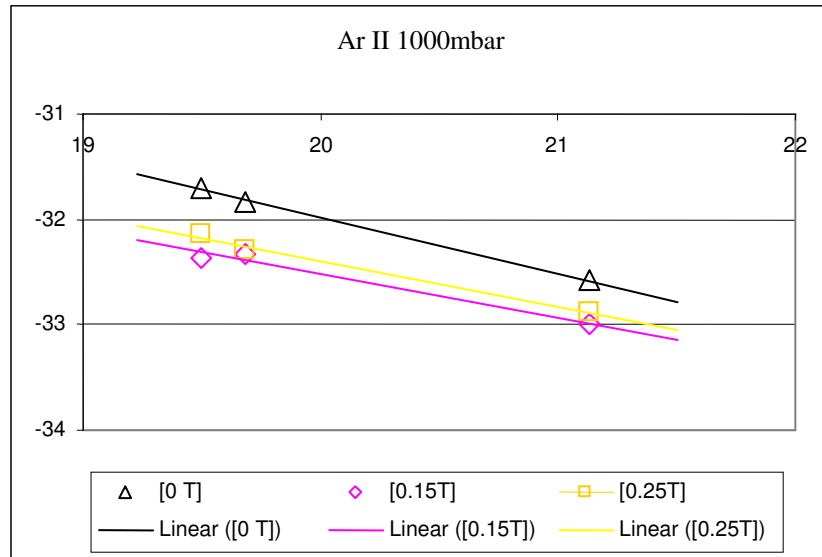


Fig. 10.27: Boltzmann plot for Ar II. Plenum pressure 1000mbar.

Conclusions

In this work the experimental activity carried out at the Alta-CPR Laboratories on MHD interaction in the shock layer above a test body immersed into a hypersonic argon flow has been described.

At several gas conditions (gas stagnation pressures of 1, 0.85 and 0.65 bar) and in a magnetic field range of 0.15-0.35, the effect of the MHD interaction with increases of the distance between the shock front and the body surface, is observed.

The MHD interaction effect seems to be limited by the low conductivity of the plasma in the boundary layer above the test body surface

The magnetic field application causes sensible variation on the Ar emission spectrum. The emission of the recorded Ar I lines in the upper part of the energy scheme decrease when the magnetic field is applied.

However, the excitation temperature calculated utilizing these levels is not affected by the magnetic field. On the other hand, the emission of the low energy line increase. Ion emission is poorly affected by the applied magnetic field.

Nomenclature

B	=	intensity of the magnetic flux density
\mathbf{B}	=	magnetic flux density vector
\mathbf{E}	=	electric field vector
E_x, E_y, E_z	=	electric field components in x-, y- and z-direction
H_{tot}	=	total specific enthalpy in the heating chamber
I_{arc}	=	arc current
\mathbf{J}	=	current density vector
J_x, J_y, J_z	=	current density components in x-, y- and z-directions
m_{dot}	=	mass flow rate
M	=	Mach number
n_{Ar}	=	argon number density at the nozzle exit
$n_{\text{Ar,sh}}$	=	argon number density within the shock layer
p_{exit}	=	gas pressure at the nozzle exit
p_{sh}	=	gas pressure within the shock layer
p_{tot}	=	stagnation pressure of gas in the heating chamber
T_{exit}	=	gas temperature at the nozzle exit
T_{sh}	=	gas temperature within the shock layer
T_{tot}	=	stagnation temperature of gas in the heating chamber
u	=	free stream gas flow velocity
u_{sh}	=	gas flow velocity in the shock layer
α_0	=	ionization degree at the nozzle inlet
β	=	angle of the shock front
β_e	=	Hall parameter of electrons
θ	=	angle of the ramp
$\rho_{e\zeta\tau}$	=	mass density of the gas at the nozzle exit
$\rho_{\sigma\eta}$	=	mass density of the gas within the shock layer
σ	=	electrical conductivity

References

- ¹ C.A. Borghi, and M. Ishikawa, New Concepts of MHD Power Generation, (invited paper), *Proc. 12th Int. Conference on MHD Electrical Power Generation*, Vol. 1, Yokohama, Japan, October 1996, pp. 38-46.
- ² V.A. Biturin, et al., Assessment of Hypersonic MHD Concepts, *28th Plasmadynamics and Lasers Conference*, Paper AIAA-97-2393, 1997.
- ³ E.P. Gurianov and P.T. Harsha, AJAX: New Directions in Hypersonic Technology, *27th Plasmadynamics and Lasers Conference*, Paper AIAA-96-4609, 1996.
- ⁴ J.T. Lineberry, et al., Prospects for MHD Flow Control for Hypersonics, *31st Plasmadynamics and Lasers Conference*, Paper AIAA-2000-3057, 2000.
- ⁵ S.O. Macheret, et al., MHD Power Extraction from Cold Hypersonic AirFlow with External Ionization, *30th Plasmadynamics and Lasers Conference*, Paper AIAA-99-4800, 1999.
- ⁶ D.J. Moorhouse and C.F. Suchomel, Exergy Methods Applied to Hypersonic Vehicle Challenge, *32nd Plasmadynamics and Lasers Conference*, Paper AIAA-2001-3063, 2001.
- ⁷ D.M. Van-Wie, et al., "Numerical Investigation of MGD Interaction in non-Equilibrium Plasma Flow in the Models of Supersonic Intake", *3rd Workshop on Magneto-Plasma-Aerodynamics in Aerospace Applications*, Moscow, April 2001.
- ⁸ R.J. Litchford, U.B. Metha, J.T. Lineberry, "Magnetohydrodynamic augmented hypersonic airbreathing propulsion", Space Transportation Day, 2000.
- ⁹ R.K. Agarwal, "Numerical simulation of compressible viscous MHD flows to study the possibility of reducing supersonic drag of blunt bodies and scramjet inlets", AFOSR Grant No.F49620-99-1-0005, 1999.
- ¹⁰ A.L. Kuranov, et al., "Modern Condition of Development and Perspective Researches of Hypersonic Technologies under the 'AJAX' Concept", *2nd Workshop on Magneto-Plasma-Aerodynamics in Aerospace Applications*, Moscow, April 2000.
- ¹¹ V.A. Zeigarnik, et al., "Mass Dimension Optimization of MHD Generators for Hypersonic Aircraft of 'AJAX' Concept", *2nd Workshop on Magneto-Plasma-Aerodynamics in Aerospace Applications*, Moscow, April 2000.

¹² S.V. Bobashev, et al., "Influence of MHD Interaction on Shock-Wave Structures in Supersonic Diffuser", *2nd Workshop on Magneto-Plasma-Aerodynamics in Aerospace Applications*, Moscow, April 2000.

¹³ W.W. Vuillermont, U. Shumlack, "Multi temperature, thermal and ion fraction effects over wedge and bluff body shapes in hypervelocity flow", *ICOPS2000*, 2000.

¹⁴ J.T. Lineberry, V.A. Bityurin et al., "Cylinder with current in Hypersonic flow", *3rd Workshop on Magneto-Plasma-Aerodynamics in Aerospace Applications*, Moscow, April 2001.

¹⁵ C.A. Borghi, M.R. Carraro, and A. Cristofolini, "Analysis of Magnetoplasmadynamic Interaction in the Boundary Layer of a Hypersonic Vehicle", *Journal of Spacecraft and Rockets*, Vol. 41, No. 4, 2004.

¹⁶ J.S. Shang, et al., "Magneto-Aerodynamic Interactions in Weakly Ionized Hypersonic Flow", *40th Aerospace Sciences Meeting & Exhibit*, paper AIAA 2002-0349, Reno, NV, 2002.

¹⁷ J.S. Shang, Recent Research in Magneto-Aerodynamics, *Progress in Aerospace Sciences*, Vol. 37, pp. 1-20, 2001.

¹⁸ V.A. Bityurin, et al., "Studies on MHD Interaction in Hypervelocity Ionized Air Flow over Aero-Surfaces", *34th Plasmadynamics and Lasers Conference*, AIAA Paper 2003-1365, Orlando, Florida, June 2003

¹⁹ V.A. Bityurin, "MHD Activity in Russia", *ILG-MHD International Workshop on Magneto-Hydro-Dynamics Applications: State of the Art*, University of Bologna, Bologna (Italy), September 2003.

²⁰ J. Lineberry, "MHD Activity in United States of America", *ILG-MHD International Workshop on Magneto-Hydro-Dynamics Applications: State of the Art*, University of Bologna, Bologna (Italy), September 2003.

²¹ F. Scortecci, F. Paganucci, L. d'Agostino, M. Andrenucci, "A New Hypersonic High Enthalpy Wind Tunnel", AIAA Paper 97-3017, July 1997.

²² F. Scortecci, F. Paganucci, L. d'Agostino, "Experimental Investigation of Shock-Wave/Boundary-Layer Interactions Over an Artificially Heated Model in Hypersonic Flow", AIAA Paper 98-1571, April 1998.

²³ A. Passaro, L. Biagioni, L. d'Agostino, "Compressibility effects in weakly turbulent hypersonic flow fields", presented at the *4th European Symposium on Aerothermodynamics for Space Vehicles*, Caserta, Italy, October 2001.

²⁴ Colonna, G., Tuttafesta, M., Capitelli, M., Giordano, D., "NO formation in one dimensional nozzle air flow with state-to-state non-equilibrium vibrational kinetics" AIAA 98-2951, April 1998.

²⁵ G.Colonna, M.Capitelli, "Selfconsistent Model of Chemical, Vibrational, Electron Kinetics in Nozzle Expansion" AIAA paper 2000-2415, and *JTHT 15*, 2001, pp. 308-316.

²⁶ G.Colonna, M.Capitelli, "The effects of electric and magnetic fields on high enthalpy plasma flows", AIAA paper 2003-4036, June 2003.

²⁷ G.Colonna, M.Tuttafesta, D.Giordano, "Numerical Methods to Solve Euler Equations in One-dimensional steady Nozzle Flow", *Computer Physics Communications*, Vol. 138, 2001, pp. 213-221.

²⁸ J.D. Anderson, *Fundamental of Aerodynamics*, 3rd editions, International edition, McGraw-Hill, New York 2001, Chapt. 9.

